FLOW VISUALIZATION FOR PLUME-SURFACE INTERACTION TESTING WITHIN LARGE-SCALE VACUUM ENVIRONMENTS AT CONDITIONS RELEVANT TO LUNAR AND MARTIAN LANDERS

N.S. Rodrigues, O.K. Tyrrell, and P.M. Danehy
NASA Langley Research Center
Hampton, VA

C.J. Eberhart, K.J. McDougal, and T.Y. Liu
NASA Marshall Space Flight Center
Huntsville, AL

T.D. Reynolds
Optical Sciences Corporation
Huntsville, AL

J.S. Rubio
Johns Hopkins University
Baltimore, MD

N. Jiang and P. Hsu
Spectral Energies, LLC
Dayton, OH

A.M. Korzun
NASA Langley Research Center
Hampton, VA

ABSTRACT

Interactions between rocket exhaust plumes and the landing surface during powered spacecraft descent on the Moon and Mars pose significant risks to the landing vehicle, landing site, and nearby infrastructure. Understanding the underlying plume-surface interaction phenomena through ground test data can provide critical insights on the sensitivities of parameters such as the spacecraft altitude and thrust. In the present work, we summarize a scaled ground test recently conducted within a 20-ft vacuum chamber environment located in the historical East Test Area at the NASA Marshall Space Flight Center. The ground test featured a Mach 5.3 inert gas plume impinging upon an instrumented flat plate. Planar laser-induced fluorescence, which is a 2D laser-based flowfield measurement technique, was performed at this test area for the first time to visualize salient flow features such as the barrel shock, stagnation shock, and wall jet. Measurements were obtained at discrete lander altitudes, made dimensionless using the nozzle exit diameter, corresponding to h/D = 10, 8, 5, 4, 3, and 2. The stagnation pressures of the plume were varied from approximately 0.04 to 1 MPa, providing sensitivity to the engine thrust of a powered spacecraft. The unique test facility allowed for *near-lunar* conditions to be obtained at initial vacuum chamber pressures less than 0.1 Pa. *Martian-relevant* measurements were also performed at ambient pressures near 600 Pa. Furthermore, a third set of measurements were obtained at so called *lunar-relevant* conditions near 3 Pa chamber pressure.

INTRODUCTION

A ground test using a scaled inert gas nozzle within a large-scale vacuum environment was conducted within the 20-ft vacuum chamber located at Test Stand 300 in the East Test Area at the NASA Marshall Space Flight Center (MSFC). The motivation for the test was to study the interactions between the rocket exhaust plume and the landing surface during powered spacecraft descent on the Moon and Mars.[1] While plume-surface interaction (PSI) testing relevant to NASA missions are generally performed using a bed of regolith simulant to mimic an unimproved surface, such as those encountered by the historic Apollo program on the Moon, the multi-phase *and* rarefied gas behavior within such flowfields have proved to be extremely difficult to model.[2]

An earlier ground test occurred within an adjacent 15-ft vacuum chamber at MSFC with several different regolith simulants to measure crater shapes and ejecta velocities at *lunar-relevant* ambient pressure conditions $P_C \sim O(3\ \text{Pa})$ and *Martian-relevant* ambient pressure conditions $P_C \sim O(600\ \text{Pa})$.[3-5] Although these measurements occurred at low ambient pressures to study the multi-phase nature of this problem at relevant conditions, the plume can generally be characterized as a continuum flow within these conditions. Subsequently, the efforts within the 20-ft vacuum chamber were focused on flowfield measurements of a supersonic jet impinging on a flat plate to study the complex gas phase flowfield involved with plume-surface interactions. The primary focus of this second effort described herein was to obtain measurements at rarefied gas conditions that could not be achieved within the 15-ft chamber, while investigating the single-phase fluid dynamics with a canonical test geometry. The unique test facility of the 20-ft vacuum chamber allowed for ambient pressure conditions $P_C \sim O(10^{-3} - 10^{-1}\ \text{Pa})$, which we denote here as *near-lunar*, rather than lunar-relevant, due to the rarefied gas behavior observed at these test conditions.

Researchers from the NASA Langley Research Center provided critical measurement design and execution of a planar laser-induced fluorescence (PLIF) system to visualize the flowfield within the 20-ft vacuum chamber. PLIF is a planar, 2D (two-dimensional) measurement technique that can be used to provide flow visualization of a targeted atom or molecule within a flowfield.[6] The PLIF variant performed for this test used seeded nitric oxide (NO), which was seeded into the inert nozzle fluid well upstream of the test article. In addition to the near-lunar measurements, flow visualization for lunar-relevant ambient pressures conditions of 2 – 4 Pa (corresponding to select test runs performed in the 15-ft vacuum chamber during the earlier test entry) and Martian-relevant ambient pressures of approximately 600 Pa were also obtained.

EXPERIMENTAL SYSTEMS

The plume-surface interaction testing reported in this paper was performed in a 20-ft diameter vacuum chamber at Test Stand 300 located within the East Test Area of NASA Marshall Space Flight Center. Figure 1 shows a CAD schematic of the vacuum chamber with the integrated test article and PLIF laser system. The test article, which was located towards the center of the vacuum chamber, featured a supersonic nozzle located on a translation stage and a flat impingement plate. Fluid lines for the nozzle test gas (heated nitrogen seeded with nitric oxide) entered the vacuum chamber via feedthrough ports. In addition to pressure instrumentation located inside the vacuum chamber, several tubes were connected to the bottom of the impingement plate and connected to pressure transducers outside of the chamber via separate feedthrough ports. A laser beam near 226 nm wavelength entered the vacuum chamber and was directed towards the test article using dichroic mirrors. A two-lens system formed the laser beam into a sheet that was approximately 140 mm tall and less than 1 mm thick at the test article. The PLIF signal was measured using an intensified sCMOS camera that was installed within a camera enclosure to protect the electronics from the harsh vacuum environment. A beam splitter plate was used to sample a small portion of the laser sheet energy and direct it towards a glass diffuser plate. The visible fluorescence from the glass diffuser was measured by a CCD camera, also located within a camera enclosure. This secondary camera was useful for monitoring the laser sheet alignment as well as energy distribution.

VACUUM CHAMER & TEST ARTICLE

The vacuum chamber featured diffusion pumps that allowed initial chamber pressures as low as $10^{-3} – 10^{-1}$ Pa to be reached. Due to accuracy limitations of a single pressure measurement instrumentation for the wide range of conditions considered, different types of pressure measurement instrumentation was required to measure the vacuum chamber pressure. A 1 Torr ($1.33 \cdot 10^2$ Pa) wall-located pressure transducer was used for near-lunar and lunar-relevant measurements, whereas a 1000 Torr ($1.33 \cdot 10^5$ Pa) wall-located pressure transducer was used for the Martian-relevant measurements. Given the very low initial vacuum pressures for the near-lunar conditions ($10^{-3} < P_{C,i} < 10^{-1}$ Pa) and the accuracy limitations of the 1 Torr transducer at these conditions, pressure data from a wall-mounted cold cathode gauge was used as the initial chamber pressure and as an offset correction for the 1 Torr transducer. A similar approach was used for the Martian-relevant conditions, where an ex-situ 10 Torr transducer was used for the initial chamber pressure measurement near 600 Pa and as an offset correction for the 1000 Torr transducer. The

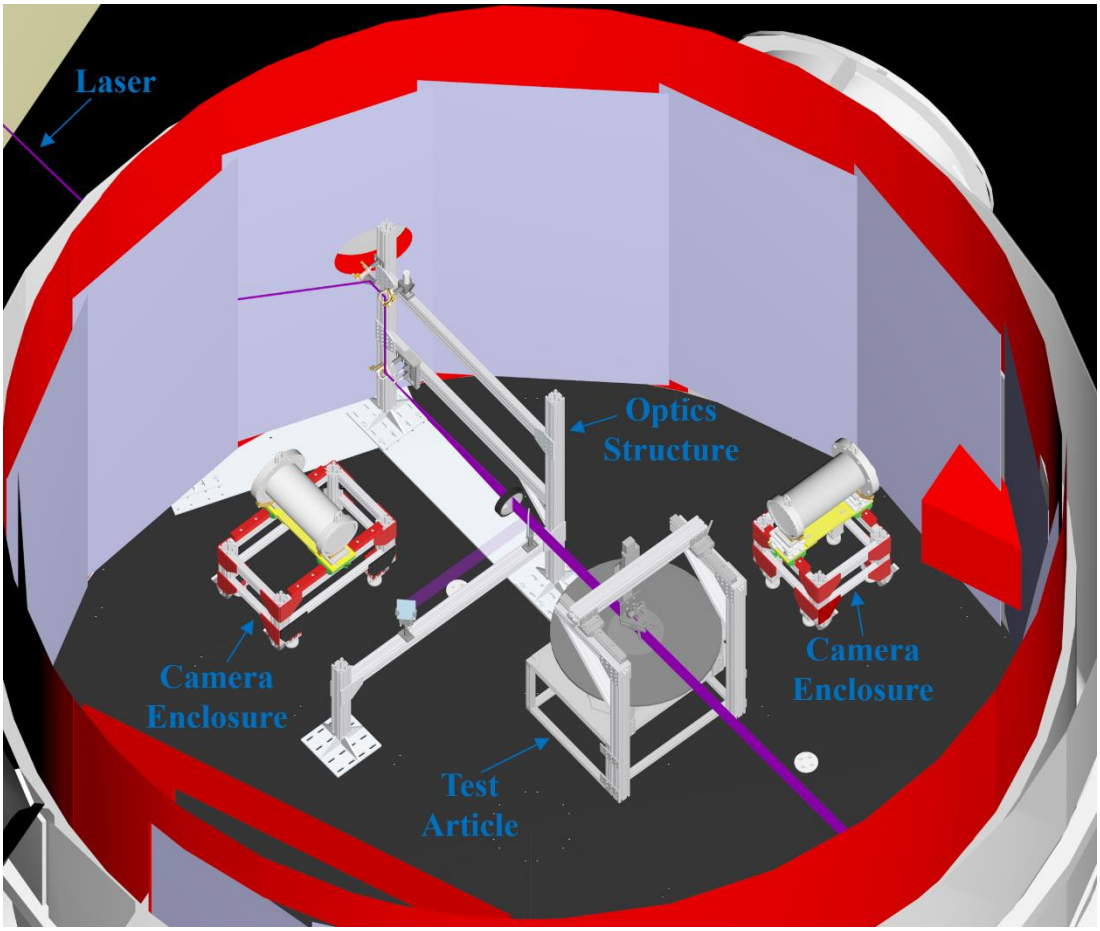

Figure 1. 3D CAD schematic showing an overview of the 20-ft vacuum chamber with the key hardware, including test article, optics support structure, and camera enclosures.

10 Torr transducer was located outside of the vacuum chamber but measured the pressure near the test article using a connecting tube. A correction for the 1 Torr transducer was not used for the lunar-relevant conditions ($2 < P_{C,i} < 3$ Pa) due to the relatively higher pressures for these conditions compared to the near-lunar conditions ($10^{-3} < P_{C,i} < 10^{-1}$). The vacuum chamber pressures were sampled by a facility data acquisition (DAQ) system operating at 100 Hz. A summary of the vacuum pressure instrumentation range and uncertainties is provided in Table 1.

The test article primarily consisted of a supersonic nozzle and a flat impingement plate that was oriented perpendicular to the nozzle flow. The supersonic nozzle, which was the same design as reported for a previous test entry in the adjacent 15-ft vacuum chamber,[1-4] featured an area ratio of approximately 31.7 and a nozzle exit diameter of approximately 1.38 cm. Facility nitrogen (N_2) heated using an in-line electric heater was used as the primary test fluid for the nozzle. A bypass loop was utilized to thermally condition the fluid component systems at elevated temperatures prior to each test run. Cartridge heaters were also located on the nozzle hardware to thermally condition the hardware prior to each run. Test runs consisted of 13 seconds between opening and closing of a remotely controlled solenoid valve, which was located downstream of the supply pressure regulators and upstream of the nozzle plenum.

Nitric oxide (NO), used as the seed gas for planar laser-induced fluorescence, was introduced to the flow path in a jet-in-crossflow configuration downstream of the electric heater and located outside of the vacuum chamber. Less than 1% NO by volume was used for the NO/N_2 mixture, which was assumed to be perfectly premixed due to the introduction of the NO seed gas well upstream of the test article at a tube length-to-diameter ratio greater than 100. Two pressure transducers, oriented 60 degrees from each other and with a maximum range of 250 psia ($1.7 \cdot 10^6$ Pa), were installed at the nozzle plenum to measure the jet stagnation pressure. An average of the two pressure transducer measurements (denoted as I and II in

Measurement	Instrument	Range	Uncertainty
Initial Vacuum Pressure, $P_{C,i}$	Wall-located cold cathode	$1.0 \cdot 10^{-6}$ – $1.0 \cdot 10^{0}$ Pa	30% reading
	Ex-situ transducer (10 Torr)	< $1.3 \cdot 10^{3}$ Pa	$6.7 \cdot 10^{-1}$ [Pa]
Vacuum Pressure, P_C	Wall-located transducer (1 Torr)	$1.3 \cdot 10^{-3}$ – $1.3 \cdot 10^{2}$ Pa	0.08% reading
	Wall-located transducer (1000 Torr)	$4.0 \cdot 10^{1}$ – $1.3 \cdot 10^{5}$ Pa	0.5% reading
Jet Stagnation Pressure, P_0	Nozzle plenum transducer I (250 psia)	< $1.7 \cdot 10^{6}$ Pa	$8.6 \cdot 10^{3}$ [Pa]
	Nozzle plenum transducer II (250 psia)		
Jet Stagnation Temperature, T_0	Nozzle plenum thermocouple (K-type)	273 – 373 K	2.2 [K]
		> 373 K	0.75% reading

Table 1. Range and uncertainty for the vacuum chamber and nozzle pressure instrumentation.

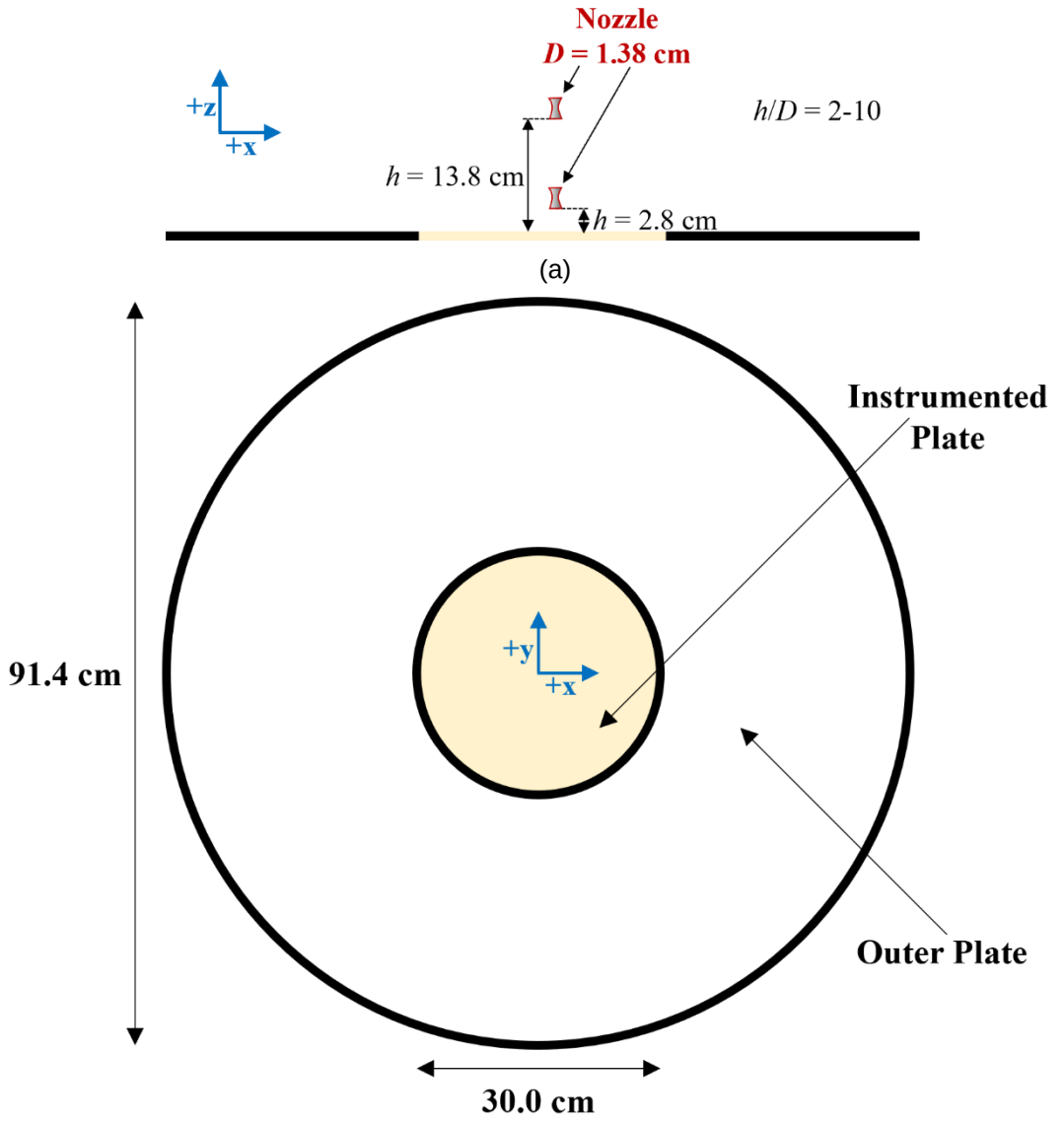

Figure 2. Schematic diagrams of the test article assembly showing: (a) range of nozzle heights over the impingement plate and (b) dimensions of the impingement plate, which consists of an instrumented inner plate and a non-instrumented outer plate.

Table 1) is used as the measured stagnation pressure P_0. Since the facility instrumentation started recording data prior to the opening of the solenoid valve, the vacuum chamber pressure was used to correct both pressure transducers in the nozzle plenum to the vacuum chamber reading before valve opening. The jet stagnation temperature was measured using a K-type thermocouple probe also located at the nozzle plenum. The range and uncertainties associated with the nozzle plenum instrumentation are also provided in Table 1. Nozzle stagnation pressure and temperature were also sampled by the facility DAQ system at 100 Hz. The nozzle hardware was installed on a remotely controlled, vacuum-compatible translation stage that allowed the nozzle height to be vertically translated relative to the impingement plate between runs without having to enter the vacuum chamber. A schematic of the test article illustrating the vertical height adjustment is shown in Fig. 2(a), indicating a vertical height adjustment range of 2.8 cm to 13.8 cm from the nozzle exit to the impingement plate. This range of vertical heights correspond to a dimensionless altitude h/D = 2-10, made dimensionless with the nozzle exit diameter D. Figure 2(b) shows a schematic of the flat impingement plate, which consists of an instrumented inner plate and an outer annular plate. The overall diameter of the outer annular plate was 91.4 cm, which corresponds to approximately 66 times the nozzle exit diameter.

The instrumented impingement plate featured an array of holes that housed separate tube lines, which were connected to low-frequency (LF) pressure transducers located outside of the vacuum chamber in a manner identical to the 10 Torr ex-situ transducer described earlier. These transducers were also sampled by the 100 Hz facility DAQ. Given the relatively long length of tube from near the center of the vacuum chamber to the transducers located outside, lag between the flow condition and the measured pressure is considerable and believed to be on the order of several seconds. Therefore, only average measurements at steady-state vacuum chamber and nozzle stagnation pressure (i.e. steady-state nozzle pressure ratio) conditions are reported in this paper. Select pressure transducers located towards the center of the plate are reported in this paper and a summary of plate locations, ranges, and uncertainties for the low-frequency pressure measurements are summarized in Table 2. The notation used for the table corresponds to the pressure locations shown schematically in Fig. 3. Several high-frequency (HF) pressure transducers were installed flush-mounted to the impingement plate surface and were sampled by a high-speed DAQ operating at 200 kHz. The plate locations, range, and uncertainties associated with the high-frequency pressure transducers are summarized in Table 3 and shown schematically in Fig. 4. The LF and HF DAQ systems were synchronized using an IRIG timecode. For the data reported in this paper from the high-frequency pressure transducers, a 100 Hz moving mean filter was applied to the high-frequency pressure measurements to reduce measurement noise and report static pressure measurements. The capability of the high-frequency pressure transducers to provide temporally resolved impingement pressure measurements, given the expected rise in vacuum chamber pressure for near-lunar and lunar-relevant vacuum pressure conditions, is an advantage over the low-frequency pressure measurements acquired using the tube lines. Although care was taken to center the nozzle over the impingement plate in both x and y directions, we estimate that the nozzle was offset in the x-direction by approximately 0.22 cm. The impingement pressure distributions are reported in this paper using an x'/D, with x' representing the corrected x-direction and D representing the nozzle exit diameter.

PLIF SYSTEM

The NASA Langley planar laser-induced fluorescence (PLIF) system used for this work primarily consisted of an Nd:YAG-pumped dye laser system, which was installed inside a mobile cart and located within a room several meters from the vacuum chamber. The second harmonic of the 10-ns pulsed Spectra-Physics® Pro-230 Nd:YAG laser at a 532 nm wavelength was used to pump a Sirah® Cobra Stretch dye laser to generate a 622 nm wavelength output beam. This output was sum-frequency mixed with the third harmonic of the YAG laser at 355-nm wavelength using a Sirah® Frequency Conversion Unit to generate approximately 4 mJ per pulse of ultraviolet (UV) tunable light near 226 nm wavelength. Further details on the PLIF system used can be found in Rodrigues *et al.*[7] Several dichroic mirrors were used to direct the laser beam into the vacuum chamber through a UV-transmissive fused silica window. Since the fused silica window was located behind the cold wall infrastructure of the vacuum chamber, a dichroic mirror installed on a vacuum-compatible, remote-controlled mirror mount was used to direct the laser beam through an opening in the cold wall. Three additional dichroic mirrors, two of which were installed on remote-controlled mirror mounts, were placed within the vacuum chamber to direct the laser beam towards the test article.

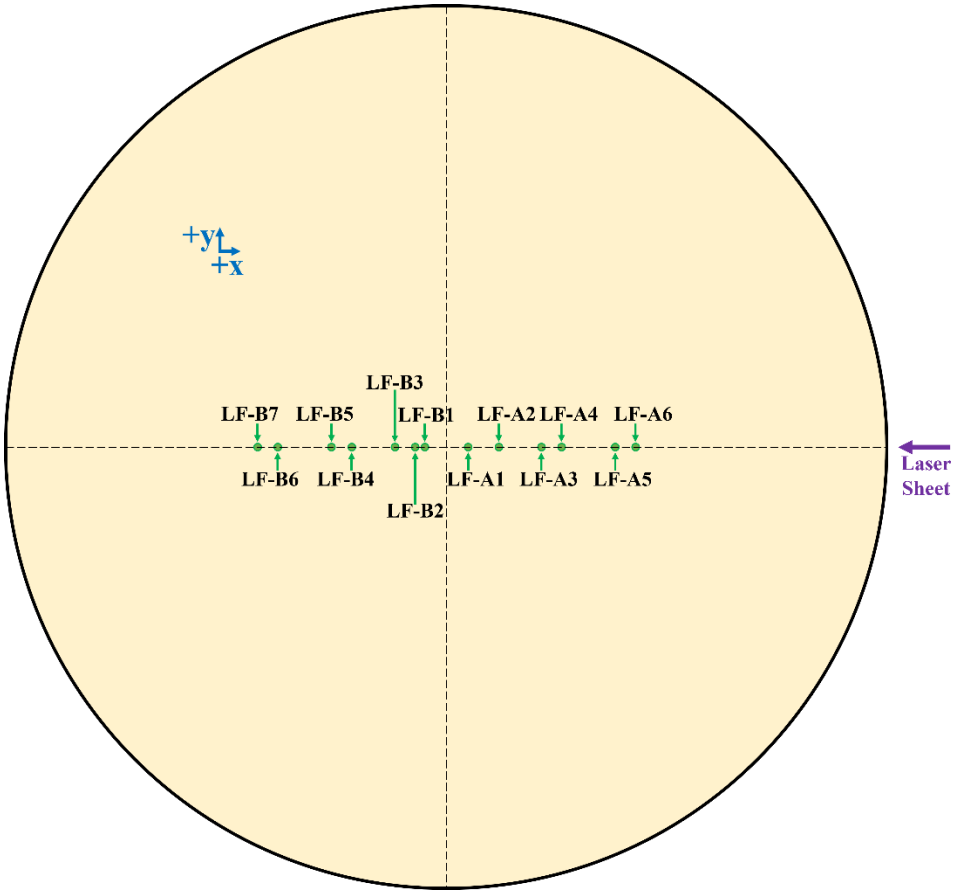

Figure 3. Schematic diagram of the instrumented plate illustrating the locations of the ex-situ low-frequency pressure measurement instrumentation using tube lines. The direction and location of the PLIF laser sheet are also indicated.

ID	Plate Location (X, Y) [cm]	Range [Pa]	Uncertainty [Pa]
LF-A1	(+0.7, 0)	$2.7 \cdot 10^{3}$	$1.3 \cdot 10^{0}$
LF-A2	(+1.8, 0)	$1.3 \cdot 10^{4}$	$6.7 \cdot 10^{0}$
LF-A3	(+3.2, 0)	$1.3 \cdot 10^{4}$	$6.7 \cdot 10^{0}$
LF-A4	(+3.9, 0)	$1.3 \cdot 10^{4}$	$6.7 \cdot 10^{0}$
LF-A5	(+5.7, 0)	$1.3 \cdot 10^{4}$	$6.7 \cdot 10^{0}$
LF-A6	(+6.4, 0)	$2.7 \cdot 10^{3}$	$1.3 \cdot 10^{0}$
LF-B1	(-0.7, 0)	$2.7 \cdot 10^{3}$	$1.3 \cdot 10^{0}$
LF-B2	(-1.1, 0)	$2.7 \cdot 10^{3}$	$1.3 \cdot 10^{0}$
LF-B3	(-1.8, 0)	$2.7 \cdot 10^{3}$	$1.3 \cdot 10^{0}$
LF-B4	(-3.2, 0)	$1.3 \cdot 10^{4}$	$6.7 \cdot 10^{0}$
LF-B5	(-3.9, 0)	$1.3 \cdot 10^{5}$	$6.7 \cdot 10^{1}$
LF-B6	(-5.7, 0)	$1.3 \cdot 10^{5}$	$6.7 \cdot 10^{1}$
LF-B7	(-6.4, 0)	$2.7 \cdot 10^{3}$	$1.3 \cdot 10^{0}$

Table 2. Location, range, and uncertainty for the low-frequency pressure measurement instrumentation connected to the impingement plate tube lines and schematically shown in Fig. 2.

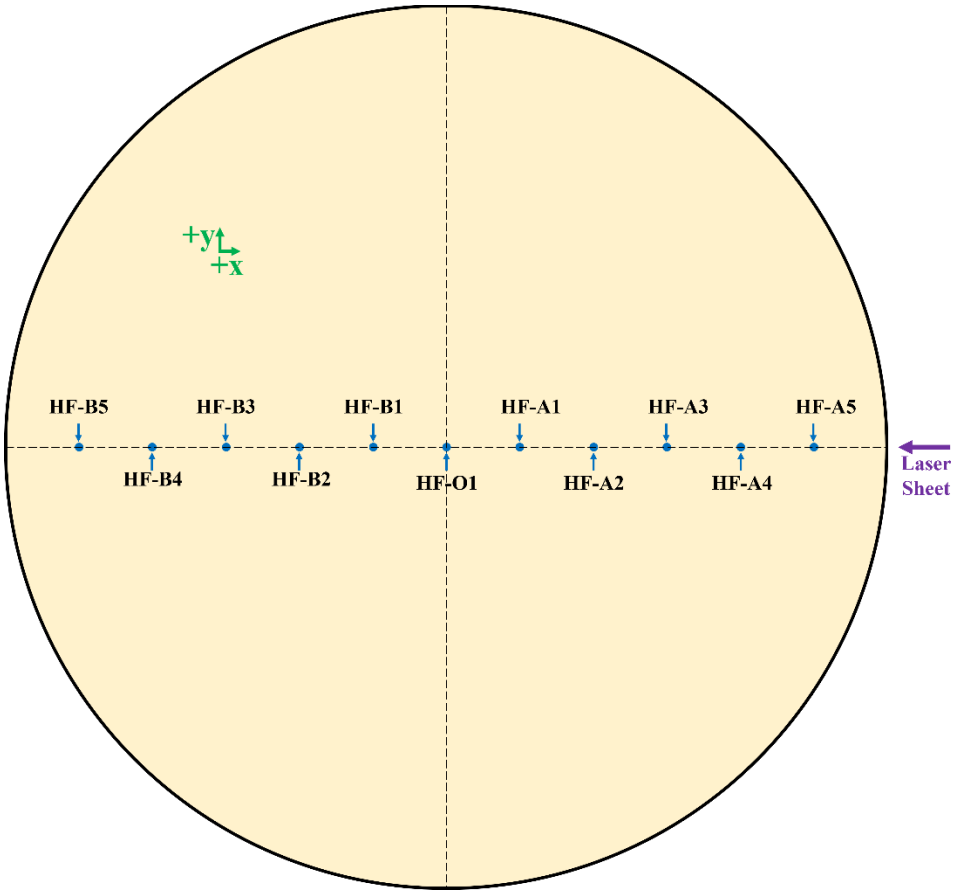

Figure 4. Schematic diagram illustrating the locations of the high-frequency pressure measurement instrumentation installed at the instrumented plate. The direction and location of the PLIF laser sheet are also indicated.

ID	Plate Location (X, Y) [cm]	Range [Pa]	Uncertainty [Pa]
HF-O1	(0, 0)	$2.4 \cdot 10^4$	$< 1.2 \cdot 10^3$
HF-A1	(0, 2.5)		
HF-A2	(0, 5.0)		
HF-A3	(0, 7.5)		
HF-A4	(0, 10.0)		
HF-A5	(0, 12.5)		
HF-B1	(0, -2.5)		
HF-B2	(0, -5.0)		
HF-B3	(0, -7.5)		
HF-B4	(0, -10.0)		
HF-B5	(0, -12.5)		

Table 3. Location, range, and uncertainty for the high-frequency pressure measurement instrumentation located on the impingement plate and schematically shown in Fig. 4.

The laser beam was formed into a laser sheet for flow visualization using a 1" diameter 25-mm focal length concave cylindrical lens that diverged the beam in the vertical direction. A 6" diameter 1-meter focal length convex spherical lens was used to collimate the beam in the vertical direction, while focusing the beam into a thin sheet in the transverse direction. The laser sheet was carefully aligned to cross through the middle of the impingement plate and the 6" diameter spherical lens was placed such that the focal plane of the laser sheet in the direction of its thickness was near the center of the impingement plate. A beam splitter plate was placed just after the 6" diameter spherical lens to sample approximately 1% of the energy in the laser sheet and direct it towards a glass diffuser plate. A 3D schematic of the PLIF laser system with the associated optics is shown in Fig. 5.

The primary PLIF camera system consisted of an intensified Andor® iStar front-illuminated scientific CMOS (sCMOS) camera, which was located within a custom camera enclosure. The camera enclosure featured a purge gas flow to mitigate overheating of the camera and a UV-transmissive fused silica window. The camera sensor featured 2560 by 2160 pixels with 6.5-micron pixel size. The camera had an 18-mm diameter WE-AGT photocathode with ultra-fast gating and used the P46 phosphor. The size of the round photocathode relative to the size of the rectangular sensor resulted in signal not being acquired for the pixels near the corners of the sensor. The intensifier gate was set to 300 ns for each of the test conditions, with the laser being fired approximately 100 ns after opening of the intensifier gate. This resulted

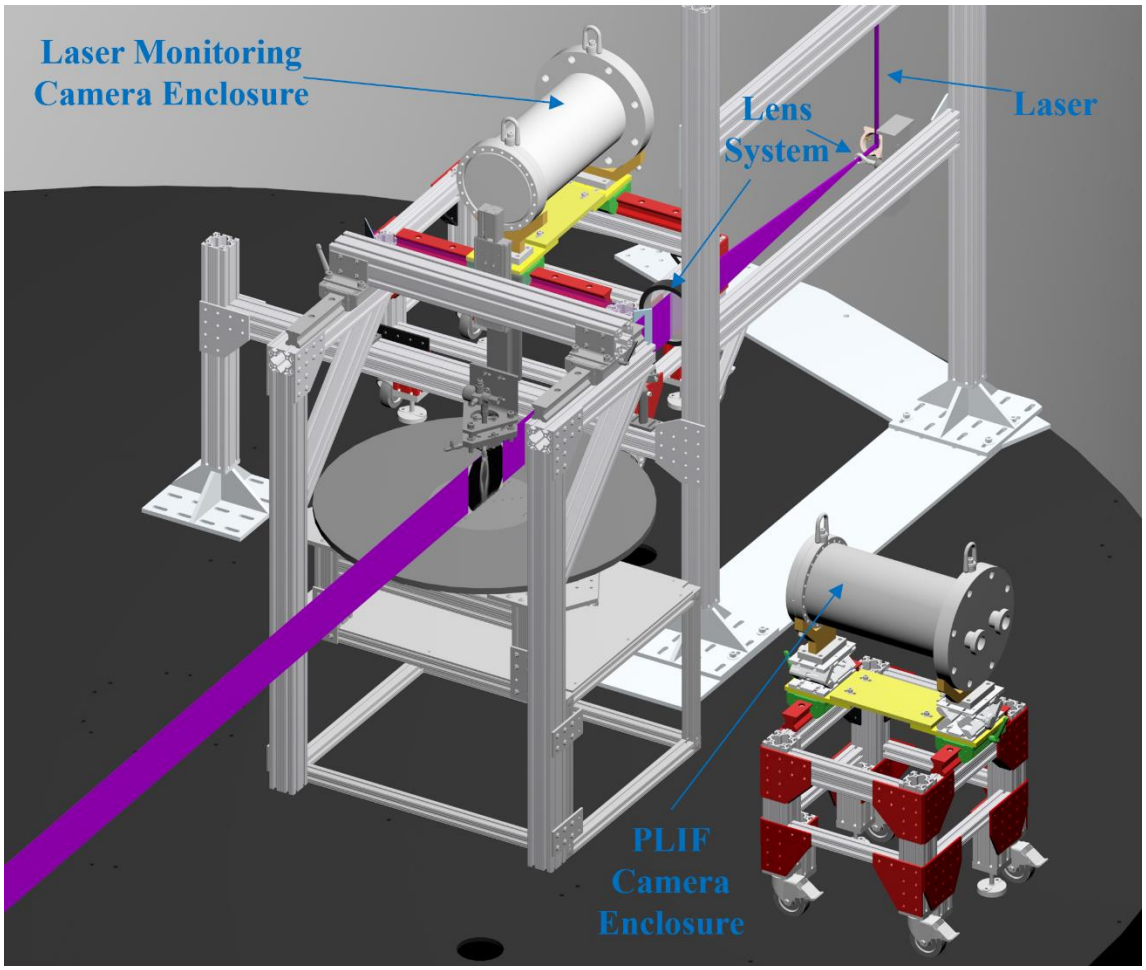

Figure 5. 3D schematic of the PLIF measurement system within the vacuum chamber. Dichroic mirrors and a lens system were mounted on a custom optics structure within the vacuum chamber and directed the laser beam to the test section and formed the laser sheet. A custom camera enclosure was also designed to protect an intensified sCMOS camera from the harsh vacuum environment.

in an effective exposure time of approximately 200 ns for each PLIF image. The field-of-view for the primary PLIF camera was centered on the nozzle in the horizontal direction and allowed the entire vertical plume to be visualized for the range of *h*/*D* parameters tested. The PLIF images were acquired using a 100-mm focal length *f*/2.8 UV camera lens. Blue fluorescence emitted by the glass diffuser plate was captured by a Cooke® SensiCam CCD camera with a 25-mm focal length *f*/1.4 visible camera lens, located within a second custom camera enclosure that also featured a purge gas flow to mitigate overheating of the camera. A glass window, rather than the more expensive UV transmissive window, was used with this camera enclosure to capture the blue light from the glass diffuser plate. This additional camera proved to be crucial for laser sheet monitoring purposes as the chamber was pumped down, since adjustments could be made with the remote mirrors to maintain laser alignment. Although not performed in the current paper, a shot-to-shot correction of the spatial variation in laser intensity across the laser sheet could be applied to the PLIF images based on the data from this camera. The auto-sequence for the test was configured such that both sCMOS and CCD cameras would automatically begin recording approximately one second before valve opening for each test run. An exposure-out signal from the sCMOS camera was also recorded by the 200 kHz DAQ in order to correlate each of the single-shot PLIF images with the data from the facility and test article instrumentation. A schematic of the camera systems is also shown in Fig. 5. Although not shown in Fig. 5, a second Andor iStar camera was installed in a Scheimpflug-configuration within its own camera enclosure during the shakedown portion of the test campaign. The primary motivation for this was to obtain a wide field-of-view PLIF image from the center of the plate to one edge.

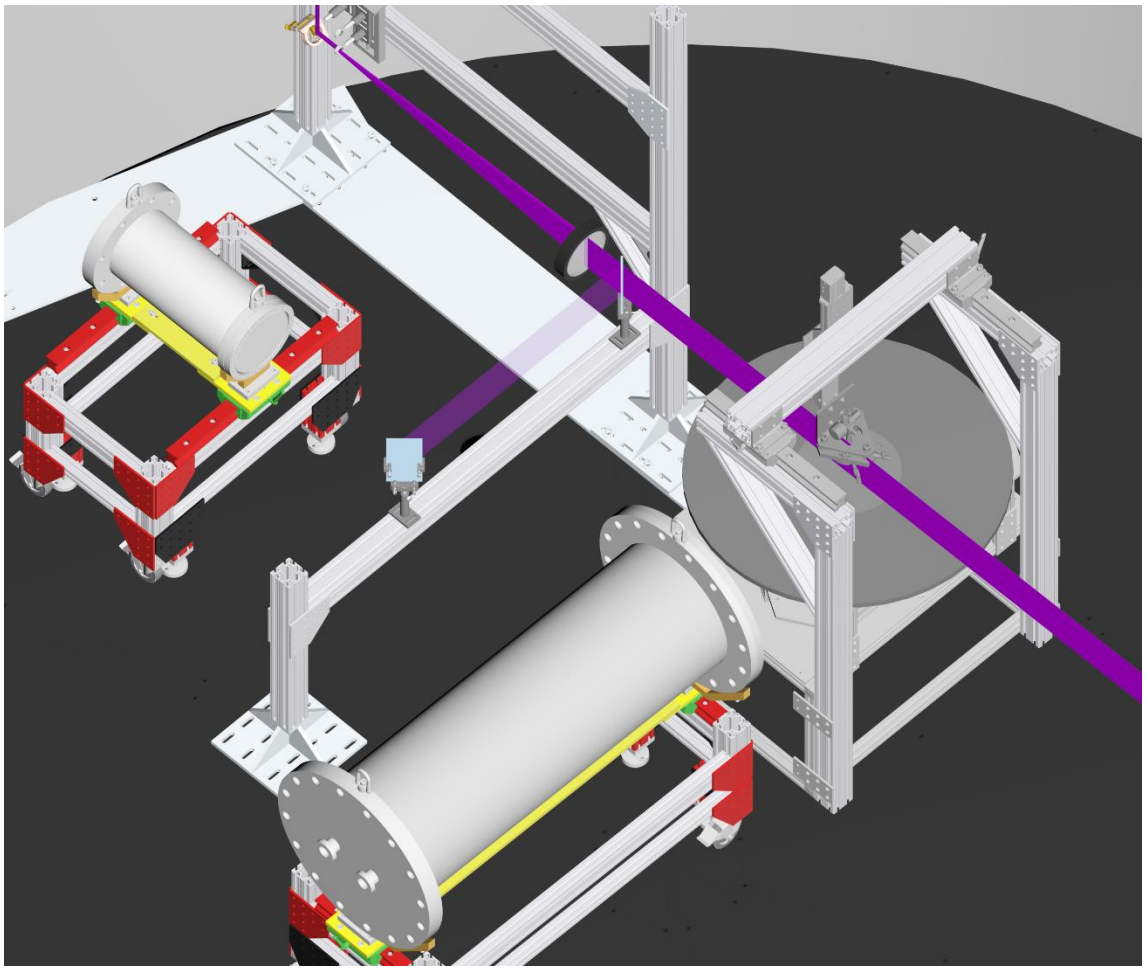

Figure 6. 3D schematic of a design to implement a high-speed PLIF system with an identical beam-path as the 10 Hz laser system, the key difference being the need for a larger camera enclosure and additional cooling capacity to contain a high-speed intensified camera system.

For the PLIF images described in this paper, the laser was tuned to the (v' = 0, v" = 0) bandhead for the A-X electronic system of nitric oxide near 226.26 nm. A long-wavelength-pass filter was used with the PLIF camera to block the majority of the laser scatter and any (v' = 0, v" = 0) fluorescence near 226 nm, while transmitting fluorescence at 230-290 nm from (v' = 0, v" = 1) through (v' = 0, v" = 5). The PLIF images were processed through a custom in-house code that corrected for the dark noise of the sensor, a flatfield correction to remove the fixed-pattern structure of the camera intensifier, and a spatial-calibration using a dewarping code. The field-of-view for the PLIF images is approximately 18.6 cm x 16.1 cm and with an image resolution of approximately 0.36 μm/pixel after applying a 2x2 pixel binning. The processed PLIF images were generated using a log-scale for the signal intensity to highlight the flow structures near the impingement plate. The 2D PLIF images were imported into Autodesk 3ds Max to visualize the data using aspects of the Virtual Diagnostics Interface (ViDI).[8] This allowed the plume visualization from the PLIF images to be presented relative to the CAD schematics of the nozzle and impingement plate.

In addition to the 10 Hz PLIF system described in this section, a measurement system design was completed to incorporate a high-speed PLIF system for plume-surface interaction visualization. The high-speed PLIF system used a burst-mode laser and an injection-seeded optical parametric oscillator system capable of high pulse energies even at high-repetition-rate such as 100 kHz. Plume measurements within laboratory-scale environments to support such an effort have also been reported by Rodrigues *et al.*[9] The completed design to implement a high-speed system within the 20-ft vacuum chamber is shown in Fig. 6. Similar to the experimental description for the 10 Hz PLIF system, the laser system was successfully installed in the room adjacent to the vacuum chamber and the laser beam path was identical to the one for the 10 Hz laser system. However, given the additional space needed for a high-speed intensified camera system near the test article, a larger camera enclosure would be required to protect the camera system. Although the design and integration of the high-speed PLIF system was completed, high-speed measurements were ultimately not acquired in the reported test entry. Obtaining measurements with such a high-speed system in the future would allow for 2D plume-surface visualization with kHz-MHz repetition-rate.

RESULTS AND DISCUSSION

In this section, the test matrix used for the overall test campaign is described in terms of the key parameters: mass flow rate $\dot{m}$, jet stagnation pressure P_0, vacuum chamber pressure P_C, and dimensionless height h/D. Four test conditions are selected from the overall test matrix that illustrate very different plume behavior for a single h/D configuration. These conditions are described in terms of the jet stagnation pressure, vacuum chamber pressure, jet stagnation temperature, and jet mass flow rate. The measured plate pressure vs. time traces from a single low-frequency pressure measurement instrumentation is also provided for each select test condition, along with a sequence of single-shot PLIF images during the initial part of the test run. The spatial distributions of surface pressure for the select conditions are also compared with the salient features observed from the PLIF flow visualization.

TEST MATRIX

The test matrix used for the entire test campaign is shown in Table 4 and is based on parametric variation of the key parameters: initial vacuum chamber pressure $P_{C,i}$, jet mass flow rate at steady state conditions $\dot{m}_{SS}$ (which corresponds to a unique steady-state jet stagnation pressure $P_{0,SS}$), and dimensionless altitude h/D. Test runs indicated with a superscript *a* correspond to test conditions also performed at the adjacent 15-ft vacuum chamber during a previous test entry, where the test effort focused on crater and ejecta measurements of a half-plane regolith bin.[1,2-4] To examine the effects of the bisecting geometry, additional test runs were completed with a *splitter plate* installed on top of the flat impingement plate. These test runs are also indicated with the *a* superscript. As mentioned in the previous section, several test runs were performed during shakedown testing with a secondary PLIF camera to image the so-called wall-jet, which is the near-wall, radial flow of gas directed away from the point of impingement. These shakedown runs overlap with the test matrix and are indicated with a *b* superscript.

In total, six different jet mass flow rates (corresponding to six different jet stagnation pressures) were tested, which can be used to characterize the sensitivity of the plume to the engine thrust. Three

		[Pa]		
$\dot{m}_{SS}$ [g/s]	**$P_{0,SS}$ [Pa]**	**$10^{-3} < P_{C,I} < 10^{-1}$**	**$2 < P_{C,i} < 3$**	**$590 < P_{C,i} < 610$**
0.32	$3.8 \cdot 10^4$	h/D = 10, 8, 5, 4, **3**, 2	$h/D = 10^{a,b}$, $3^{a,b}$	$h/D = 10^{a}$, $\mathbf{3}^{a}$
0.65	$7.9 \cdot 10^4$	h/D = 10, 3		
1.2	$1.5 \cdot 10^5$	h/D = 10, 8, 5, 4, 3, 2		
2.4	$2.8 \cdot 10^5$	h/D = 10, 3		
5.1	$6.1 \cdot 10^5$	h/D = 10, 3		
8.1	$9.7 \cdot 10^5$	h/D = 10, 8, 5, 4, **3**, 2	$h/D = 10^{a}$, 3^{a}	$h/D = 10^{a}$, 8, 5, 4, $\mathbf{3}^{a,b}$, 2

[a] Test matrix runs corresponding to runs with regolith in the 15-ft chamber and 20-ft chamber splitter plate test runs.
[b] Test matrix runs corresponding to runs with the secondary PLIF camera during 20-ft camber shakedown tests.

Table 4. Test matrix summary for flow visualization runs with the flat impingement plate. The jet mass flow rate at steady state conditions is denoted by $\dot{m}_{SS}$. $P_{C,i}$ and $P_{0,SS}$ represent the initial pressure of the vacuum chamber and steady-state jet stagnation pressure, respectively. Whereas h/D represents the altitude of the jet relative to the plate, made dimensionless with the nozzle exit diameter. Test conditions highlighted in this paper are indicated with bold red in the table.

distinct ranges for the initial vacuum chamber pressure were also targeted, corresponding to near-lunar ($10^{-3} < P_{C,i} < 10^{-1}$ Pa), lunar-relevant ($2 < P_{C,i} < 3$ Pa), and Martian-relevant ($590 < P_{C,i} < 610$ Pa). Six different dimensionless altitudes (h/D = 10, 8, 5, 4, 3, and 2) were targeted for four distinct jet and vacuum chamber combinations, with the majority of the jet and vacuum chamber combinations limited to h/D = 10 and 3. The test matrix is represented in Fig. 7 with graphs that correspond to the initial vacuum chamber pressure $P_{C,i}$ vs. steady-state jet stagnation pressure $P_{0,SS}$ for the different h/D values investigated in the overall test matrix. Also shown in this graph is the so-called 3rd critical of the supersonic nozzle, which corresponds to the supersonic design condition and provides a separation of three different supersonic flow regimes: overexpanded, perfectly expanded, and underexpanded. The test matrix was designed to include one targeted overexpanded condition for the h/D = 10 and 3 altitudes, which corresponds to the low flow rate at the Martian-relevant vacuum chamber condition. All of the other targeted conditions correspond to an underexpanded jet.

This current paper focuses on four different jet and vacuum pressure conditions that are all at a dimensionless altitude h/D = 3. Two test conditions are shown for the near-lunar vacuum environment, where the vacuum chamber was pumped down to its lowest limit. These two test conditions correspond to the lowest and highest steady-state mass flow rates (or steady-state jet stagnation pressures) for the jet within the near-lunar pressure environment. The other two test conditions correspond to the Martian-relevant vacuum chamber pressure near 600 Pa, and also correspond to the lowest and highest mass flow rates of the jet tested.

SELECT TEST CASES

Data for the selected near-lunar test conditions corresponding to $\dot{m}_{SS}$ = 0.32 g/s, $P_{0,SS} = 3.8 \cdot 10^4$ Pa, and $10^{-3} < P_{C,i} < 10^{-1}$ Pa for a dimensionless altitude of h/D = 3 are shown in Figs. 8 and 9. Fig. 8(a) shows the jet stagnation pressure and the vacuum chamber pressure vs. time for the duration of the test run. The time t = 0 corresponds to the received trigger signal of the PLIF camera, which was automatically triggered approximately one second before the opening of the solenoid valve as part of the test run auto-sequence. The first detection of flow on the PLIF camera was consistently observed at a timestamp corresponding to approximately t = 1.2 s after camera trigger (or within 100 ms after valve opening) for all test runs. Steady-state conditions for the jet flow were consistently observed at approximately t = 1.3 s after camera trigger (or within 100-200 ms after valve opening) based on the PLIF flow visualization. However, the measured pressure within the nozzle plenum typically required 1-2 seconds after valve opening to reach steady state. The measured pressure right after valve opening is believed to be a static pressure reading rather than a stagnation pressure reading, as the relatively high-pressure gas upstream of the valve is likely directly flowing through the plenum and out of the nozzle. This delay can be at least partially attributed to the relatively large volume for the nozzle plenum. We believe that the nozzle plenum fills up within 3 seconds after valve opening, resulting in the dynamic pressure ($\frac{1}{2}\rho u^2$) reaching a negligible value and the measured reading being a true stagnation pressure. The measured reading is indicated in

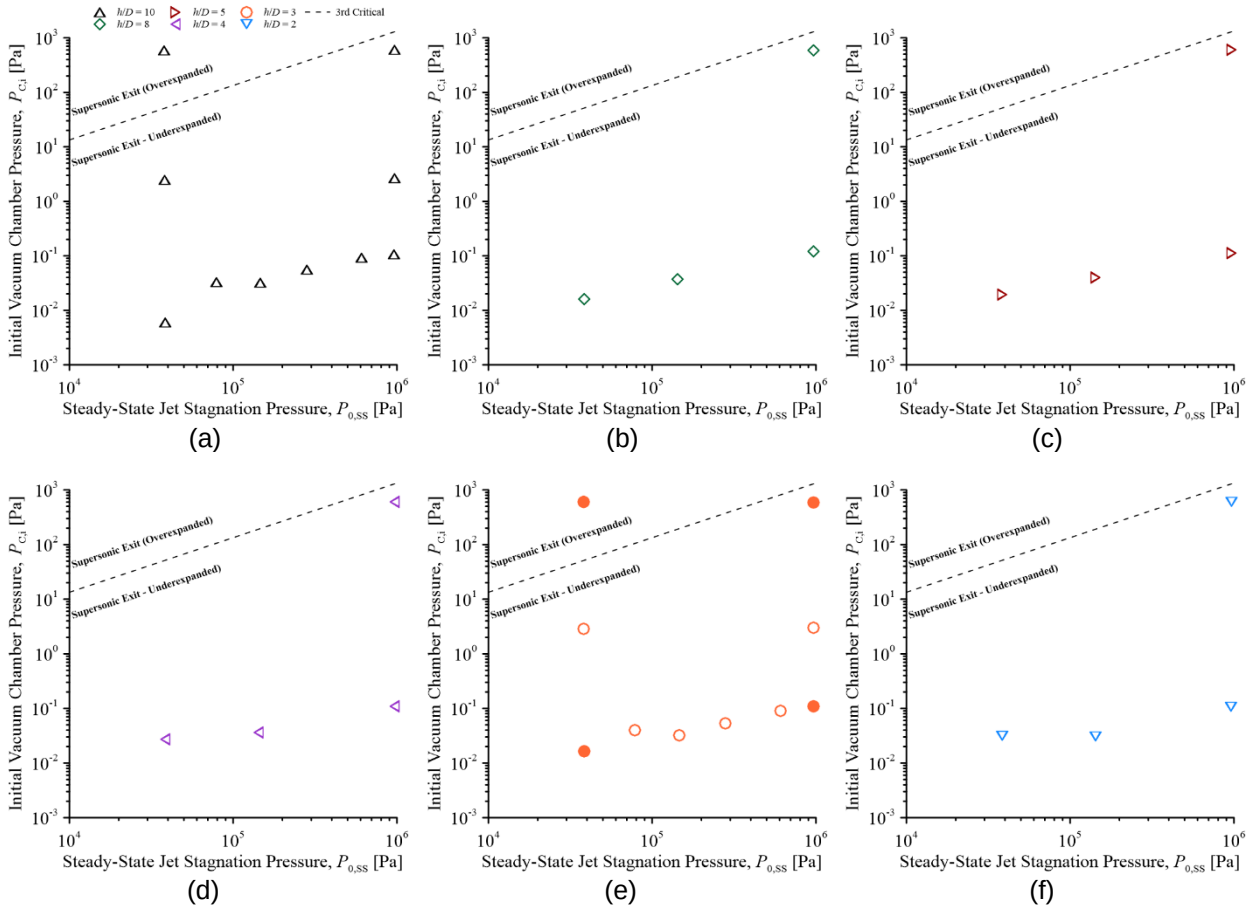

Figure 7. Representation of the text matrix runs in terms of initial vacuum chamber pressure $P_{C,i}$ vs. steady-state jet stagnation pressure $P_{0,SS}$ for the six different dimensionless altitudes of: (a) h/D = 10, (b) h/D = 8, (c) h/D = 5, (d) h/D = 4, (e) h/D = 3, (f) h/D = 2. Also shown in the dashed line is the estimated 3rd Critical based on a Mach number M = 5.3 and a specific heat ratio γ = 1.4. Test conditions highlighted in this paper are indicated as solid symbols within (e).

Fig. 8(a) with open symbols and is referred to as a *measured* P_0 throughout this paper. The measured stagnation pressure from approximately three seconds after valve opening to valve closing was linearly fit to account for the slight consistent decrease in stagnation pressure over the test run. The linear fit was extrapolated to 100-200 ms after valve opening and this is shown as a *corrected* P_0 within 8(a) and throughout this paper.

At this very low initial vacuum chamber pressure condition, the jet flow into the vacuum chamber increased the vacuum chamber pressure by approximately two orders of magnitude despite the relatively low mass flow rate of 0.32 g/s and the relatively large vacuum chamber volume. The corresponding jet stagnation temperature and mass flow rate are shown in Fig. 8(b). The jet stagnation temperature was relatively constant near 500 K. The nozzle pressure ratio P_0/P_C and the measured plate pressure from a low-frequency pressure transducer near the plate center (LF-A1) are shown in Fig. 8(c) as a function of time. Based on this pressure trace, it appears that there was a significant lag for the low-frequency plate pressure measurement for this test condition, which corresponds to the combination of lowest jet stagnation pressure and lowest vacuum chamber pressure within the test matrix. The image sequence of the first six PLIF images are shown in Fig. 9. The nozzle flow appeared to be very diffused for these images, which can be attributed to the highly rarefied flow conditions. The images do not appear to vary significantly within this sequence. Although the plume appears to be relatively uniform, some evidence of a jet core can be seen in these images. A relatively flat stagnation shock can also be observed near the impingement plate, with the wall jet emanating from the plate at a noticeable angle.

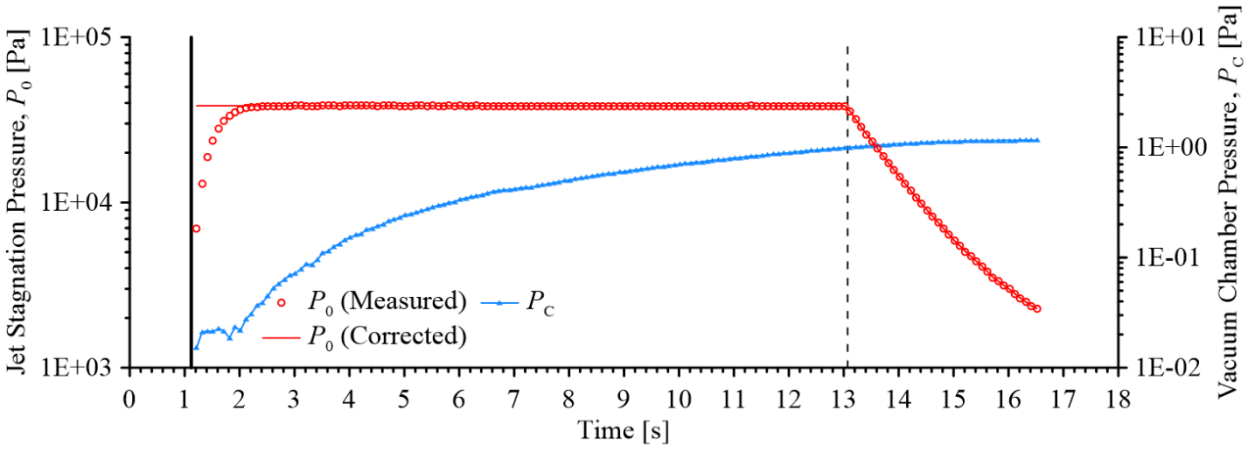

(a)

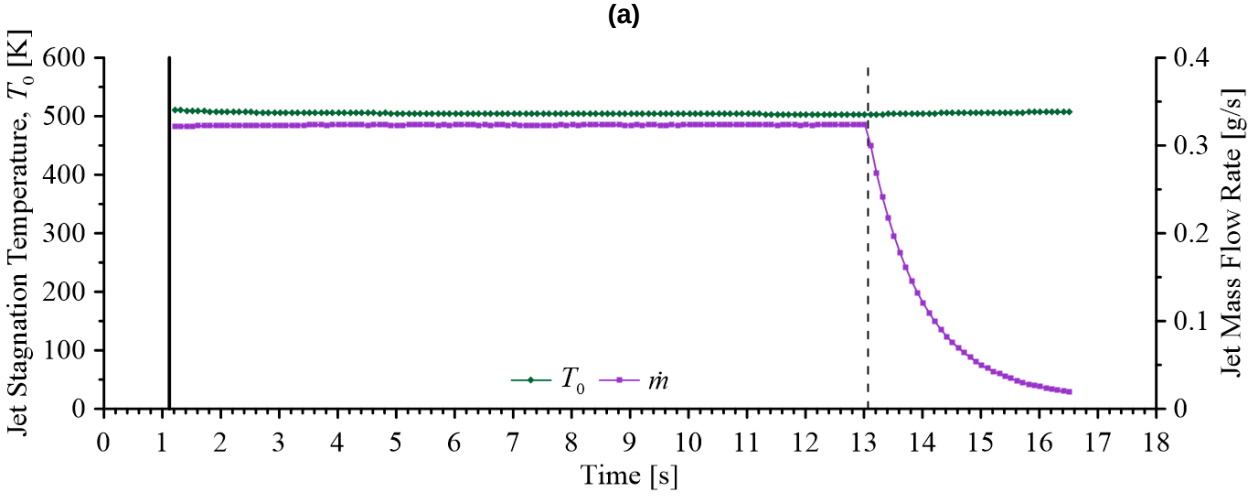

(b)

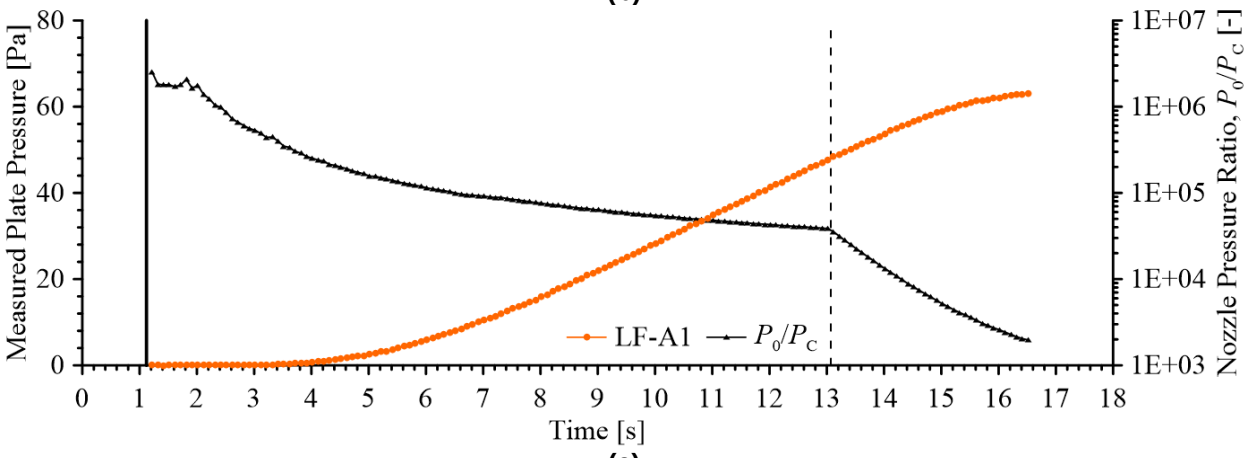

(c)

Figure 8. Sequence of a test run at conditions corresponding to $P_{C,i}$ = 1.5·10^{-2} Pa, $P_{0,SS}$ = 3·8·10^{4} Pa, and *h*/*D* = 3: (a) vacuum chamber pressure and jet stagnation pressure vs. time, (b) jet stagnation temperature and mass flow rate vs. time, and (c) low-frequency plate pressure LF-A1 and nozzle pressure ratio vs. time. The solid vertical line indicates solenoid valve opening and the dashed vertical line indicates valve closing.

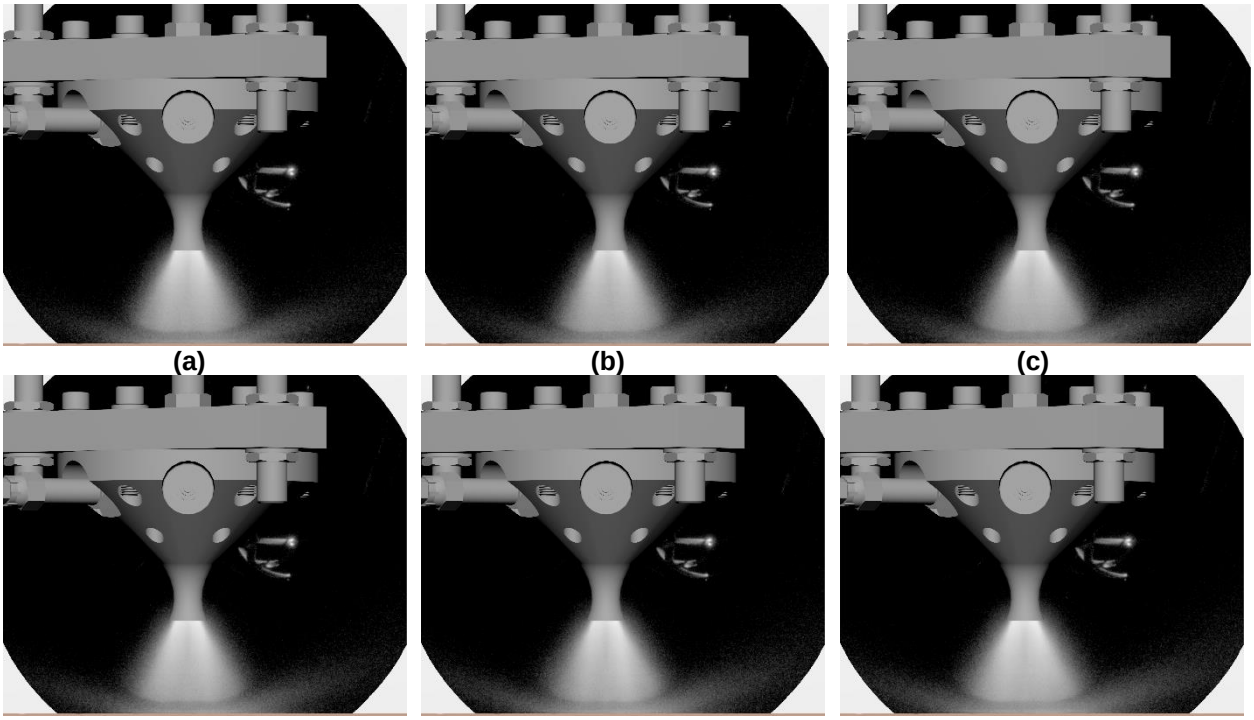

Figure 9. Sequence of PLIF images, shown in logarithmic scale, with respect to time stamp in Fig. 18 corresponding to $P_{C,i} = 1.5 \cdot 10^{-2}$ Pa, $P_{0,SS} = 3.8 \cdot 10^{4}$ Pa, and $h/D = 3$: (a) $t = 1.2$ s, (b) $t = 1.3$ s, (c) $t = 1.4$ s, (d) $t = 1.5$ s, (e) $t = 1.6$ s, (f) $t = 1.7$ s.

Figures 10 and 11 describe the near-lunar test condition corresponding to the highest steady-state mass flow rate and jet stagnation pressure of $\dot{m}_{SS} = 8.1$ g/s and $P_{0,SS} = 9.7 \cdot 10^{5}$ Pa, respectively, with the vacuum chamber initially at the near-lunar condition of $10^{-3} < P_{C,i} < 10^{-1}$ Pa and the dimensionless altitude at $h/D = 3$. This test condition corresponds to the combination of highest jet stagnation pressure and lowest vacuum chamber pressure of the test matrix. Figure 10(a) shows the jet stagnation pressure reaching steady-state conditions, while the vacuum chamber pressure continues to rise during the test run in a manner similar to Fig. 8(a). As shown in Fig. 10(b) and similar to 8(b), the jet stagnation temperature also appears to be nearly constant over the run. Likely due to the higher jet stagnation pressures at this test condition, the measured plate pressure does appear to reach steady state over the test run as seen in Fig. 10(c). However, because of the continual change in the nozzle pressure ratio during the run, the measured plate pressure cannot be attributed to one single nozzle pressure ratio. This is also illustrated in Fig 10(c). This test run highlights the limitations of the low-frequency pressure measurements to quantitively match the measured plate pressure to a single test parameter for this highly transient near-lunar condition. Detailed study of the lag in the tubes in-between the impingement plate and the pressure transducers may provide more quantitative metrics of the impingement pressure to the range of nozzle pressure ratios encountered during the test run. Nevertheless, high-bandwidth measurements such as those obtained with the high-frequency pressure transducers flush-mounted on the impingement plate or the single-shot PLIF measurements are the preferred measurements for such a transient environment.

Fig. 11 shows the sequence of the first six PLIF images corresponding to the early part of the run at this test condition. The higher jet pressure at this condition leads to the visualization of several very clear flow features: jet core, triangular stagnation shock, oblique shock near the wall-jet, and a wall-jet with large scale structures. Interestingly, the jet boundary out of the nozzle appears to be rather diffuse, which can be attributed to the rarefied vacuum chamber conditions. Similar to the PLIF images for the test condition reported in Fig. 9, the salient features of the flowfield do not appear to significantly change with time. Furthermore, it is noteworthy that although the range of nozzle pressure ratios for the images reported in Fig. 9 and Fig. 11 are similar, $P_0/P_C \sim O(10^4\text{-}10^6)$, it is clear that these flowfields are very

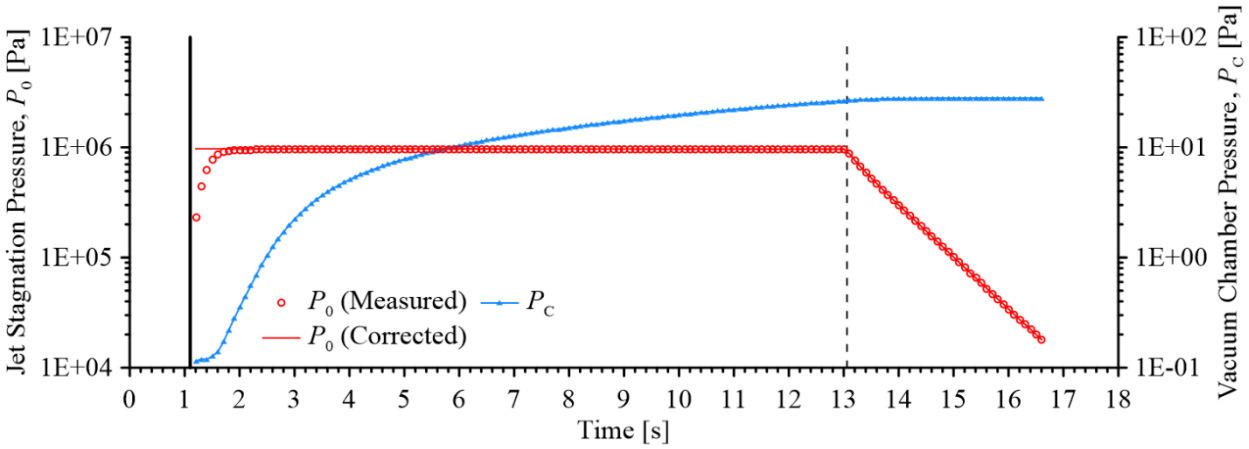

(a)

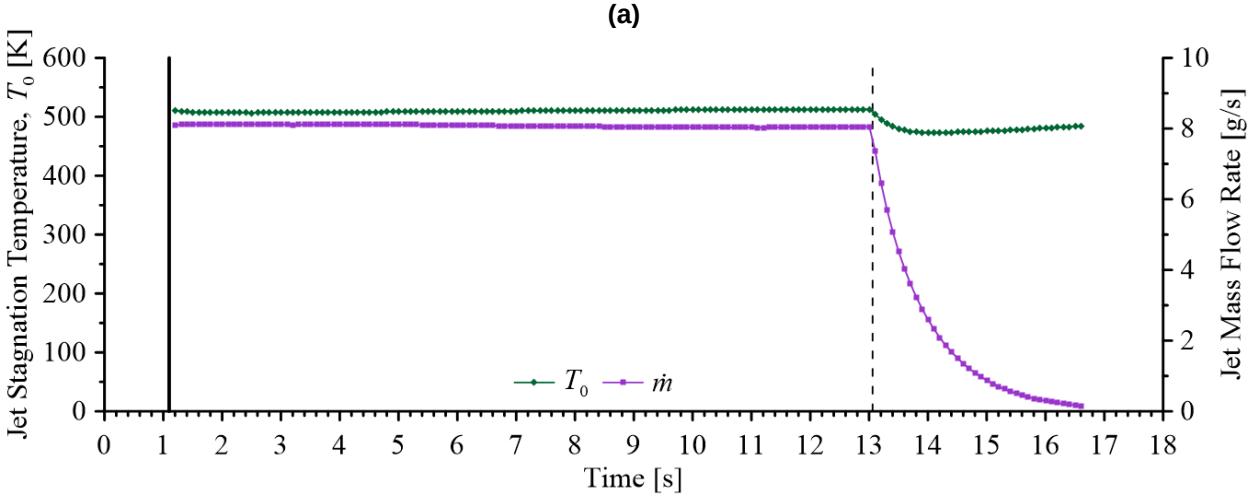

(b)

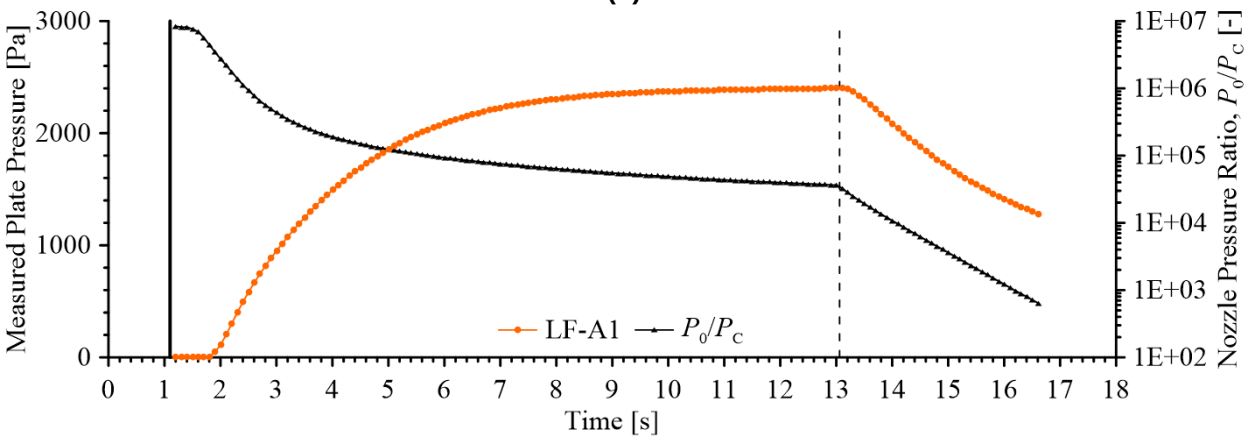

(c)

Figure 10. Sequence of a test run at conditions corresponding to $P_{C,i} = 1.2 \cdot 10^{-1}$ Pa, $P_{0,SS} = 9.7 \cdot 10^{5}$ Pa, and $h/D = 3$: (a) vacuum chamber pressure and jet stagnation pressure vs. time, (b) jet stagnation temperature and mass flow rate vs. time, and (c) low-frequency plate pressure LF-A1 and nozzle pressure ratio vs. time. The solid vertical line indicates solenoid valve opening and the dashed vertical line indicates valve closing.

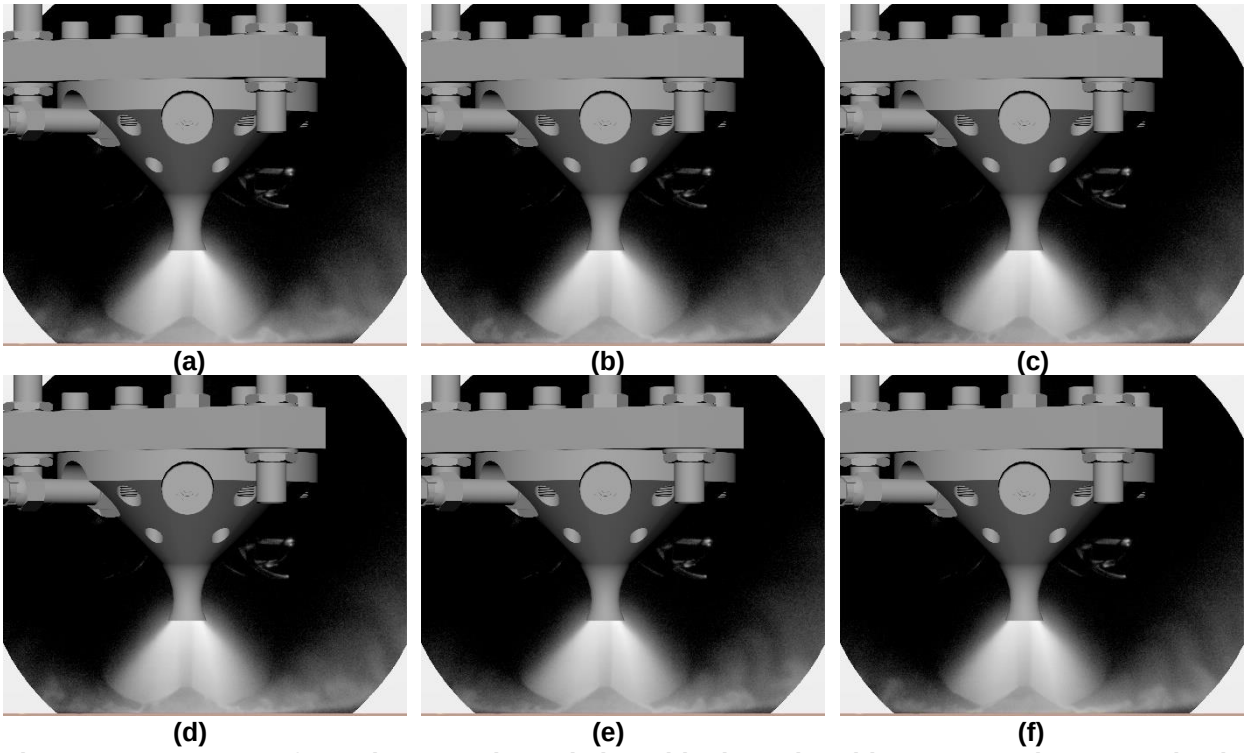

Figure 11. Sequence of PLIF images, shown in logarithmic scale, with respect to time stamp in Fig. 10 at conditions corresponding to $P_{C,i} = 1.2 \cdot 10^{-1}$ Pa, $P_{0,SS} = 9.7 \cdot 10^{5}$ Pa, and $h/D = 3$: (a) $t = 1.2$ s, (b) $t = 1.3$ s, (c) $t = 1.4$ s, (d) $t = 1.5$ s, (e) $t = 1.6$ s, (f) $t = 1.7$ s.

different. This perhaps highlights the significant influence of other dimensionless variables for this plume-surface flowfield.

Data for the Martian-relevant test condition corresponding to $\dot{m}_{SS} = 0.32$ g/s, $P_{0,SS} = 3.8 \cdot 10^{4}$ Pa and $590 < P_{C,i} < 600$ Pa at a dimensionless altitude $h/D = 3$ are described in Figs. 12 and 13. This test condition corresponds to the combination of lowest jet stagnation pressure and highest initial vacuum chamber pressure of the test matrix. The jet stagnation pressure vs. time trace for this Martian-relevant vacuum chamber condition in Fig. 12(a) appears to be very similar to the near-lunar vacuum chamber condition for the same $\dot{m}$ and $P_{0,SS}$ flow condition in Fig. 8(a). The temporal profiles for the jet stagnation temperature and the jet mass flow rate over the test run also appear to the very similar in Fig. 12(b) to those of Fig. 8(b). However, one clear difference between this Martian-relevant test condition and the corresponding near-lunar test condition is the relatively steady-state vacuum chamber pressure during the entire test run as seen in Fig. 12(a). The nozzle pressure ratio is therefore relatively steady over the test run at this condition, as seen in Fig. 12(c). The measured pressure near the plate center using the LF-A1 pressure transducer reaches a plateau during the run. Therefore, the measured plate pressure distribution from the low-frequency pressure instrumentation may be quantitatively paired to a steady-state nozzle pressure ratio. The sequence of PLIF images during the early portion of the test run are shown in Fig. 13. Another difference between this test condition and the previous two test conditions for the near-lunar case is the supersonic jet operating within the overexpanded jet regime. A highly collimated jet can be seen in Fig. 13, with evidence of flow separation within the nozzle, along with the presence of a horizontal shock downstream of the nozzle exit. The flow appears to be rather unsteady near the nozzle plate, with the formation of a *tree-trunk* like structure at the impingement plate. Evidence of an unsteady wall jet can also be seen in the PLIF images. Similar to the lunar-relevant conditions described earlier, the salient flow features such as the jet diameter appear to be similar over time for the sequence of images.

Figures 14 and 15 describe the Martian-relevant test condition corresponding to the highest mass flow rate and jet stagnation pressure of $\dot{m}_{SS} = 8.1$ g/s and $P_{0,SS} = 9.7 \cdot 10^{5}$ Pa, respectively, with the vacuum chamber at the Martian-relevant condition of $590 < P_{C,i} < 600$ Pa and the $h/D = 3$. Once again, the jet

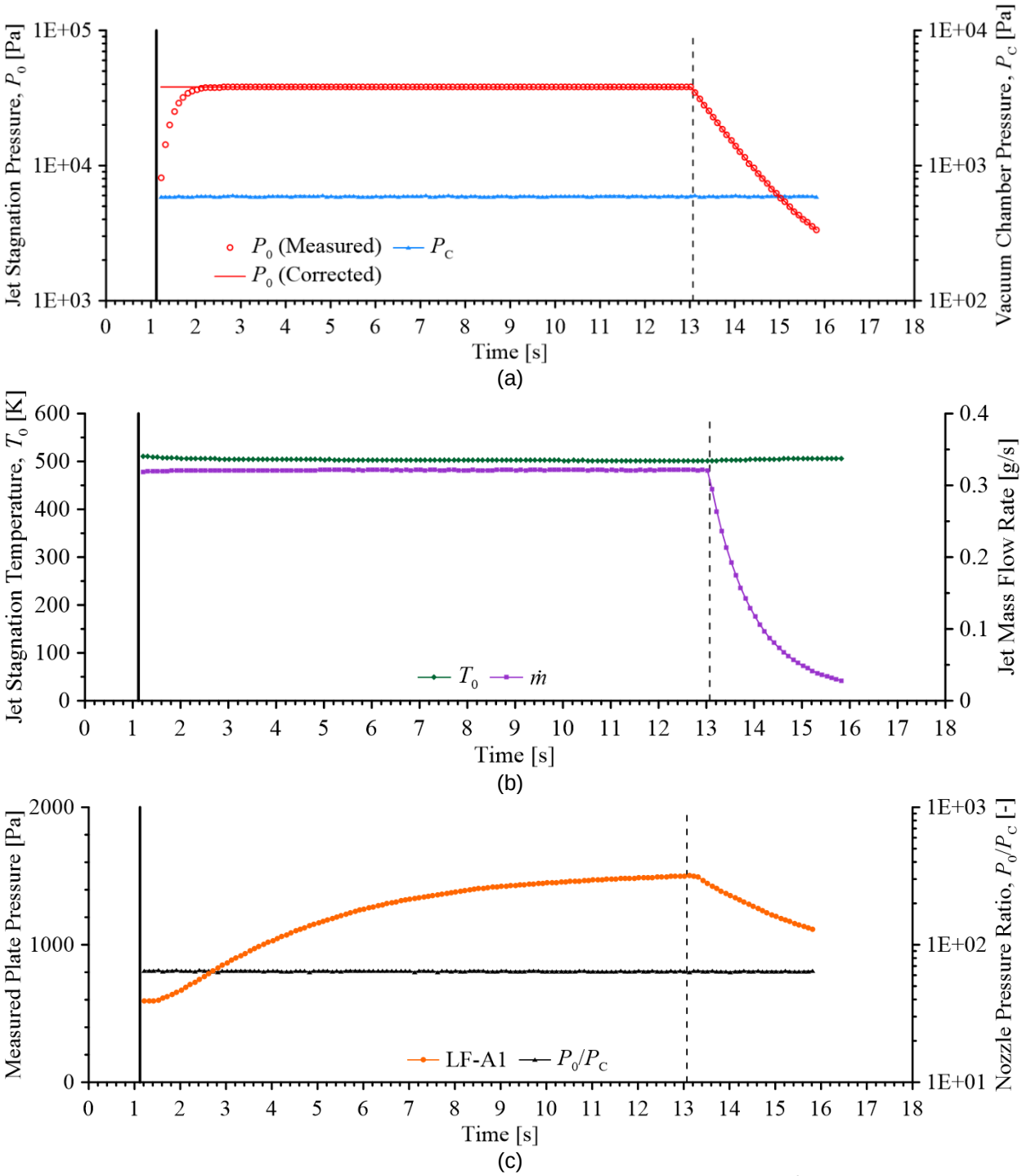

Figure 12. Sequence of a test run at conditions corresponding to $P_{C,i} = 5.9 \cdot 10^2$ Pa, $P_{0,SS} = 3.8 \cdot 10^4$ Pa, and $h/D = 3$: (a) vacuum chamber pressure and jet stagnation pressure vs. time, (b) jet stagnation temperature and mass flow rate vs. time, and (c) low-frequency plate pressure LF-A1 and nozzle pressure ratio vs. time. The solid vertical line indicates solenoid valve opening and the dashed vertical line indicates valve closing.

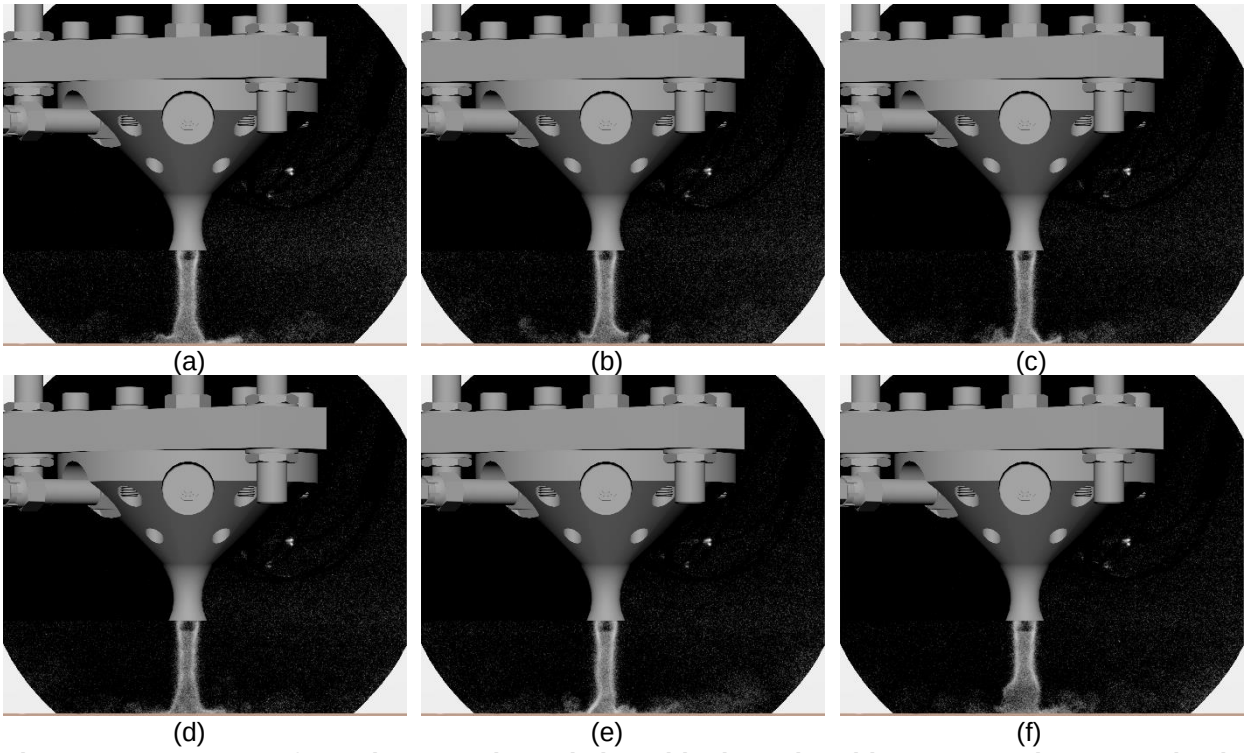

Figure 13. Sequence of PLIF images, shown in logarithmic scale, with respect to time stamp in Fig. 12 at conditions corresponding to $P_{C,i} = 5.9 \cdot 10^2$ Pa, $P_{0,SS} = 3.8 \cdot 10^4$ Pa, and $h/D = 3$: (a) $t = 1.2$ s, (b) $t = 1.3$ s, (c) $t = 1.4$ s, (d) $t = 1.5$ s, (e) $t = 1.6$ s, (f) $t = 1.7$ s.

stagnation pressure time trace in Fig. 14(a) as well as the jet stagnation temperature and jet mass flow rate time traces in Fig. 14(b) show very similar behavior to the corresponding near-lunar condition in Figs. 10(a) and 10(b). For this Martian-relevant case, however, the vacuum chamber pressure also appears to remain steady despite the relatively high mass flow rate as seen in Fig. 14(a). Similar to the Martian-relevant case of $\dot{m} = 0.32$ g/s described, the steady-state jet stagnation pressure and steady-state vacuum pressure allow a steady-state nozzle pressure ratio to be reached. The combination of highest stagnation pressure and highest vacuum chamber in terms of the test matrix, however, resulted in the saturation of the low-frequency pressure transducer near the jet center (LF-A1, LF-B1, LF-B2, and LF-B3), which have a maximum range of approximately $2.7 \cdot 10^3$ Pa (20 Torr). Therefore, for the pressure time trace shown in Fig. 14(c), the $1.3 \cdot 10^4$ Pa (100 Torr) pressure transducer denoted as LF-A2 is used. The sequence of PLIF images corresponding to the early portion of the run at this test condition are shown in Fig. 15. Once again, the salient flow features appear to be similar over the sequence of images at this test condition. These salient flow features, which are clearly identifiable in the PLIF images shown in Fig. 15, include the jet core, oblique stagnation shock, and the wall-jet, which also shows large-scale structures.

The measured spatial distribution of the impingement pressure for the two Martian-relevant cases using the low-frequency pressure transducers are shown in Fig. 16(a). Since these can be categorized as average or low-bandwidth measurements, the average PLIF images for the two corresponding cases are shown in Fig. 16(b) and 16(c). The average PLIF images correspond to a sample of 100 images acquired in the 10 seconds before jet shut-off. The spatial coordinates for the pressure distribution in Fig. 16(a) are denoted using the dimensionless axis of x'/D rather than x/D, as an offset corresponding to 0.22 cm was used to correct for the nozzle offset with respect to the center of the impingement plate in the x direction. This offset was determined using the PLIF images acquired with the splitter plate configuration, which was briefly described with the previous test matrix section. As mentioned earlier, four pressure transducers near the center of the plate over-ranged for the $P_0/P_C = 1.6 \cdot 10^3$ condition and therefore indicate a plate pressure greater than $2.7 \cdot 10^3$ Pa (20 Torr) at these locations. The other pressure transducers at this condition, however, show the plate pressure radially decreasing away from the center, particularly within

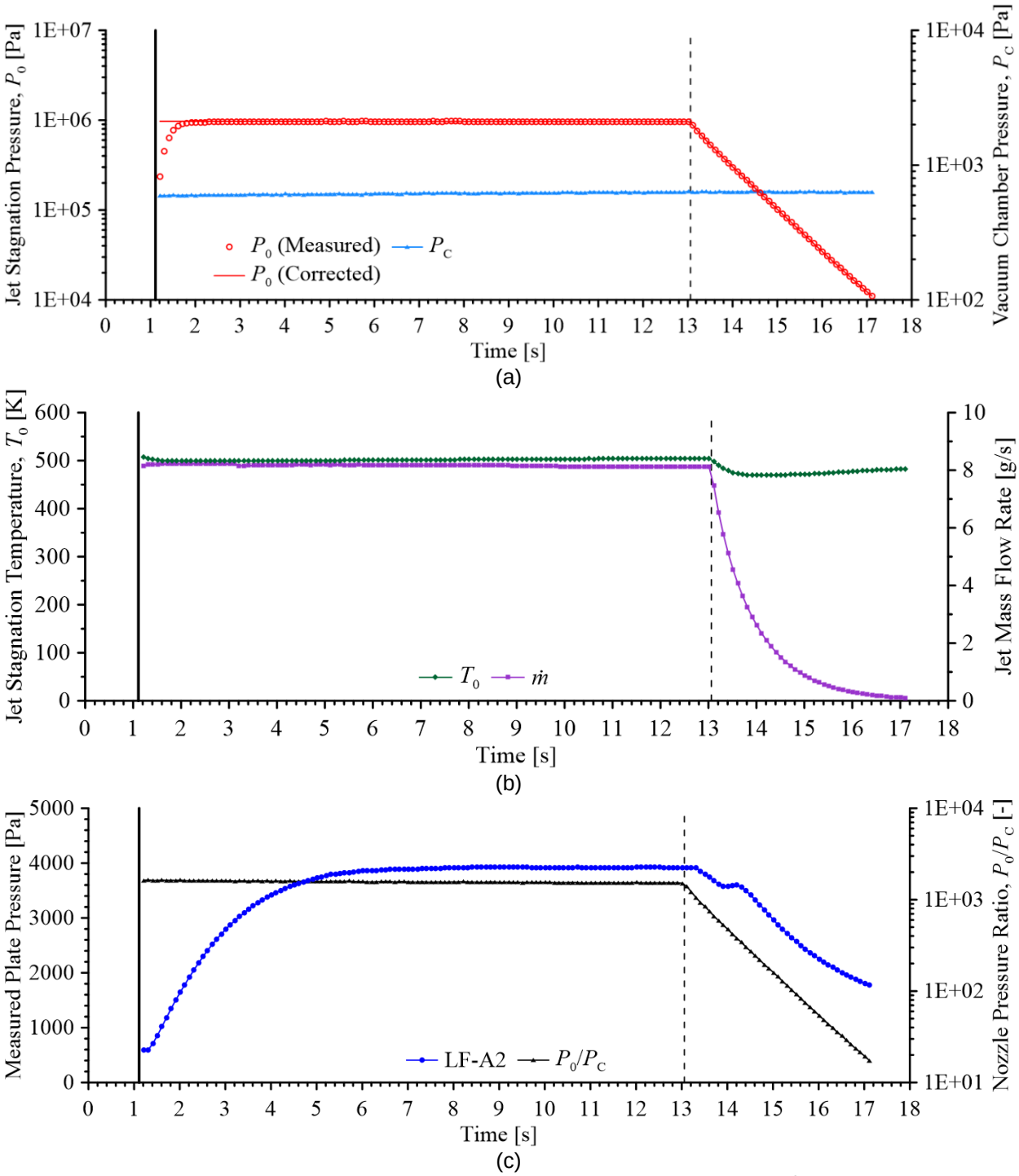

Figure 14. Sequence of a test run at conditions corresponding to $P_{C,i} = 6.0 \cdot 10^2$ Pa, $P_{0,SS} = 9.7 \cdot 10^5$ Pa, and $h/D = 3$: (a) vacuum chamber pressure and jet stagnation pressure vs. time, (b) jet stagnation temperature and mass flow rate vs. time, and (c) low-frequency plate pressure LF-A2 and nozzle pressure ratio vs. time. The solid vertical line indicates solenoid valve opening and the dashed vertical line indicates valve closing.

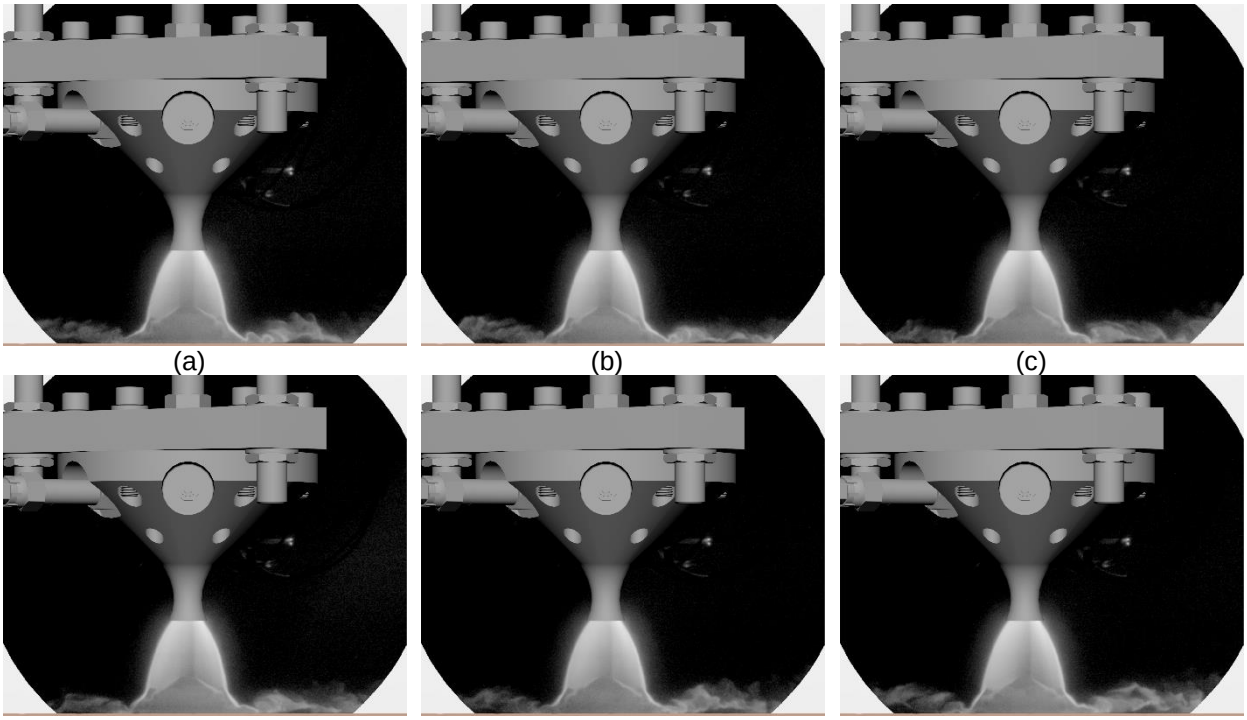

Figure 15. Sequence of PLIF images, shown in logarithmic scale, with respect to time stamp in Fig. 14 at conditions corresponding to $P_{C,i} = 6.0 \cdot 10^2$ Pa, $P_{0,SS} = 9.7 \cdot 10^5$ Pa, and $h/D = 3$: (a) $t = 1.2$ s, (b) $t = 1.3$ s, (c) $t = 1.4$ s, (d) $t = 1.5$ s, (e) $t = 1.6$ s, (f) $t = 1.7$ s.

the $\pm 1.5 < x'/D < \pm 3$ range. Interestingly, near $x'/D = \pm 3$, the plate pressure appears to be lower than the vacuum chamber pressure, which may correspond to a low-pressure (suction) region below the lifted wall-jet. This structure in the pressure profile at the plate was also previously observed in the impingement pressure measurements of Inman *et al.*[10] The plate pressure distribution for the $P_0/P_C = 6.4 \cdot 10^1$ condition reveals a double-peak profile, with the peaks occurring near $x'/D = \pm 0.5$. The higher plate pressure away from the centerline can be attributed to the high-velocity jet boundary impinging on the flat plate. This multi-peaked spatial structure in the pressure profile was also observed by Inman *et al.*[10]

The plate pressure distribution from the high-frequency pressure transducers for the near-lunar conditions described earlier are shown in Figs. 17 and 18. The high-bandwidth nature of these measurements allow the pressure profile to be correlated to a particular PLIF image, despite the transient nature of the test. Perhaps due to the relatively sparse spatial density of these transducers, a similar pressure profile can be observed for the two conditions despite the very different flow structures visualized from the PLIF. A measurement near the jet center was not obtained for the lower mass flow rate condition due to an issue with the sensor during this particular test run. At the higher mass flow rate condition, the pressure transducer was observed to overrange, indicating an impingement pressure greater than $2.4 \cdot 10^4$ Pa. Nevertheless, the presence of an impingement pressure several x'/D from the jet centerline indicates the progression of the wall-jet flow even in these low vacuum environments. This adds further evidence for the potential of the wall-jet created during a lunar landing to travel far from the landing site and disturb nearby infrastructure, especially when considering ejecta transport that such a wall-jet may produce.

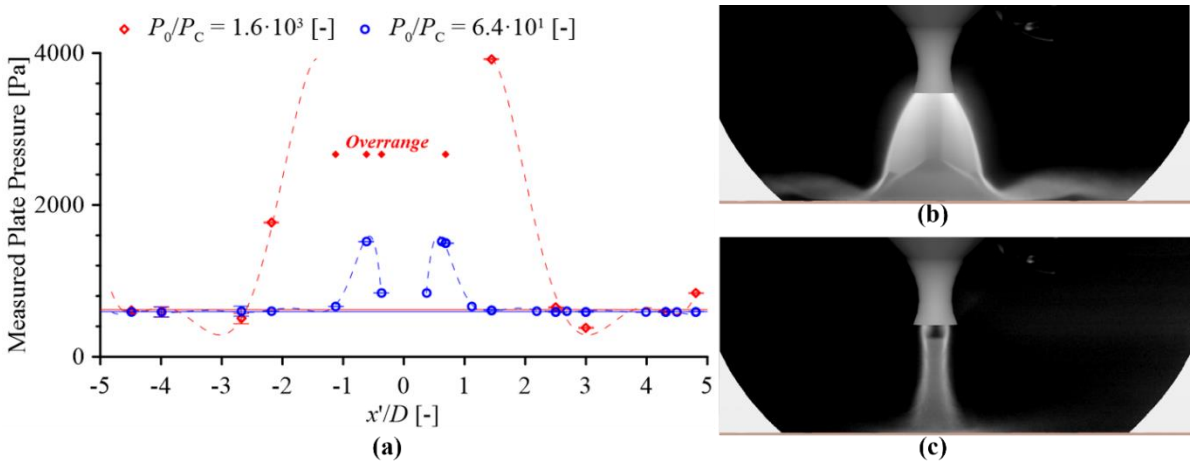

Figure 16. (a) Measured plate pressure vs. *x*'/D for two different nozzle pressure ratios at Martian conditions. The corresponding average PLIF image, shown in logarithmic scale, is shown for the two conditions with: (b) $P_0/P_C = 1.6 \cdot 10^3$ and (c) $P_0/P_C = 6.4 \cdot 10^1$. The average vacuum chamber pressure corresponding to these conditions are illustrated by the horizontal lines.

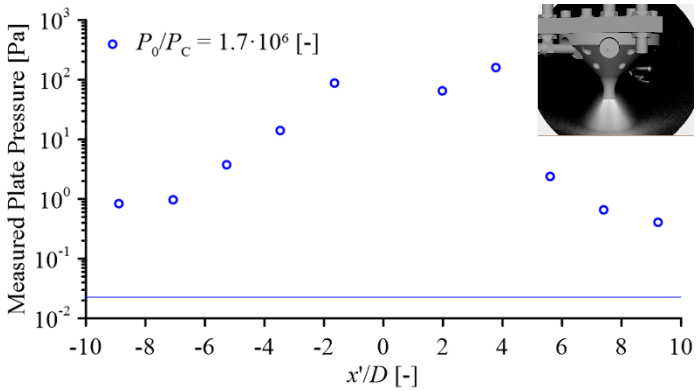

Figure 17. Measured plate pressure using the high-frequency pressure instrumentation vs. *x*'/D for near-lunar conditions corresponding to $P_0/P_C = 1.7 \cdot 10^6$ ($\dot{m}$ = 0.32 g/s). The PLIF image, shown in logarithmic scale, corresponding to this pressure distribution is shown in the inset. The vacuum chamber pressure is illustrated by the horizontal line.

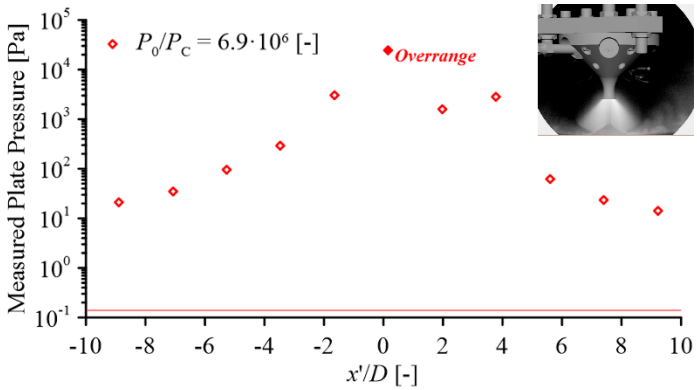

Figure 18. Measured plate pressure using the high-frequency pressure instrumentation vs. *x*'/D for near-lunar conditions corresponding to $P_0/P_C = 6.9 \cdot 10^6$ ($\dot{m}$ = 8.1 g/s). The PLIF image, shown in logarithmic scale, corresponding to this pressure distribution is shown in the inset. The vacuum chamber pressure is illustrated by the horizontal line.

SUMMARY AND CONCLUSIONS

In the present work, we provide an overview of a scaled inert gas test performed within a large-scale vacuum environment to study the flowfield aspect of plume-surface interaction. Measurements, particularly laser-based measurements, within large-scale ground test facilities typically utilize complex experimental systems and this paper serves as an overview of the completed ground test. The overall test matrix for the ground test is described and representative data is provided for four combinations of the nozzle and vacuum chamber conditions. Although the selected test conditions are shown at a single dimensionless altitude h/D = 3, distinct features of the flowfield based on the planar laser-induced fluorescence images are observed for the four conditions. In addition to providing a validation dataset for predictive simulations, the flow visualization and pressure data obtained with the flat plate configuration may be used to explain some of the trends observed with the previous test entry with regolith simulants.

ACKNOWLEDGMENTS

The authors wish to acknowledge the support of the *Plume Surface Interaction* project, which was funded by the NASA Space Technology Mission Directorate (STMD) Game Changing Development (GCD) program with S. Harris from NASA Marshall Space Flight Center (MSFC) serving as project manager. Funding for NJ and PH of Spectral Energies, LLC to collaborate for the ground test effort was granted by the ARMD and STMD through a Phase II Small Business Innovation Research (SBIR) award under Contract No. 80NSSC20C0099. The authors thank Dr. M. Mehta from MSFC for setting the initial direction of this work and also wish to acknowledge the technical input on test design and direction from Dr. J. West, Dr. A. Weaver, and T. Shurtz from MSFC. The efforts of the entire staff at MSFC-ET10 are also acknowledged, especially those of Dr. J. Sisco, K. Miasek, and K. Thompson. The authors also thank H. Ripley from the NASA Langley Research Center (LaRC) for assistance with preparation and shipment of PLIF equipment to the test facility. Finally, N.S. Rodrigues thanks Dr. T. Fahringer from LaRC for assistance with PLIF image dewarping.

REFERENCES

1. Korzun, A. M., Eberhart, C. J., West, J., Liever, P., Weaver, A., Mantovani, J., Langton, A., Kemmerer, B., and Atkins, A., **Design of a Subscale, Inert Gas Test for Plume-Surface Interactions in a Reduced Pressure Environment**, in AIAA SciTech Forum, AIAA 2022-1808, AIAA, San Diego, CA (Jan. 2022).

2. West, J., Liever, P., Weaver, A., Shurtz, T.P., Gale, M., Krolick, W.C., and Griffin, L.W., **Overview of the Predictive Simulation Capability Element of the Plume Surface Interaction Project**, in AIAA SciTech Forum, AIAA 2022-2319, AIAA, San Diego, CA (Jan. 2022).

3. Eberhart, C. J., West, J., and Korzun, A. M., **Overview of Plume-Surface Interaction Data from Subscale Inert Gas Testing at NASA MSFC Test Stand 300 Vacuum Facilities**, in AIAA SciTech Forum, AIAA 2022-1808, AIAA, San Diego, CA (Jan. 2022).

4. Rubio, J. S., Gorman, M., Diaz-Lopez, M., and Ni, R., **Plume-Surface Interaction Physics Focused Ground Test 1: Setup and Preliminary Results**, in AIAA SciTech Forum, AIAA 2022-1809, AIAA, San Diego, CA (Jan. 2022).

5. Diaz-Lopez, M., Gorman, M., Rubio, J. S., and Ni, R., **Plume-surface Interaction Physics Focused Ground Test 1: Diagnostics and Preliminary Results**, in AIAA SciTech Forum, AIAA 2022-1810, AIAA, San Diego, CA (Jan. 2022).

6. Danehy, P. M., Weisberger, J., Johansen, C., Reese, D., Fahringer, T., Parziale, N. J., Dedic, C., Estevadeordal, J., and Cruden, B. A., **Non-Intrusive Measurement Techniques for Flow Characterization of Hypersonic Wind Tunnels**, NATO STO Manuscript on Hypersonic Freestream Characterization, 2018.

7. Rodrigues, N. S., Bathel, B. F., and Danehy, P. M., Jiang, N., Hsu, P., Leicht, J., and Roy, S., **A comparison of NO laser-induced fluorescence models at conditions relevant to supersonic and hypersonic flows**, in AIAA SciTech Forum, AIAA 2022-0897, AIAA, San Diego, CA (Jan. 2022).

8. Schwartz, R. J. and Fleming, G. A., **Virtual Diagnostics Interface: Real Time Comparison of Experimental Data and CFD Predictions for a NASA Ares I-Like Vehicle**, in *22nd International Congress on Instrumentation in Aerospace Simulation Facilities*, IEEE, Pacific Grove, CA (Nov. 2007).

9. Rodrigues, N. S., Danehy, P. M., Jiang, N., Hsu, P., Leicht, J., and Roy, S., **100 kHz High-Spectral-Resolution NO-PLIF Measurements for Compressible Flows**, in AIAA SciTech Forum, AIAA 2023-0405, AIAA, National Harbor, MD (Jan. 2023).

10. Inman, J. A., Danehy, P. M., Nowak, R. J., and Alderfer, D. W., **Fluorescence Imaging Study of Impinging Underexpanded Jets**, in 46th AIAA Aerospace Sciences Meeting and Exhibit, AIAA 2008-619, AIAA, Reno, NV (Jan. 2008).